REVIEW

Graphene's photonic and optoelectronic properties – A review

A J Wirth-Lima[1,†], P P Alves-Sousa[2], and W Bezerra-Fraga[1,2]

[1] Department of Physics, Federal Institute of Education, Science and Technology of Ceará Campus Sobral, Ceará, Brazil
[2] Postgraduate Program in Electrical Engineering and Computing Federal University of Ceará (U.F.C.) Sobral, Ceará, Brazil

(Received 18 October 2019; revised manuscript received 27 November 2019; accepted manuscript online 9 December 2019)

Due to its remarkable electrical and optical properties, graphene continues to receive more and more attention from researchers around the world. An excellent advantage of graphene is the possibility of controlling its charge density, and consequently, the management of its conductivity and dielectric constant, among other parameters. It is noteworthy that the control of these properties enables the obtaining of new optical/electronic devices, which would not exist based on conventional materials. However, to work in this area of science, it is necessary to have a thorough knowledge regarding the electrical/optical properties of graphene. In this review paper, we show these graphene properties very well detailed.

Keywords: absorbance, conductivity, dielecric constant, dispersion relation

PACS: 78.20.–e, 78.20.–e, 31.15.es, 11.55.Fv **DOI:** 10.1088/1674-1056/ab5fc2

1. Introduction

Due to their excellent electrical and optical properties, graphene and other two-dimensioanl metamaterials are attacking tremendous interest from the international scientific community. It is possible to control its charge density, and consequently, the management of its conductivity and dielectric constant, among other parameters. Hence, obtaining new electronic and optoelectronic devices is possible, which would not exist based on the conventional materials. Researchers have already presented many graphene-based optoelectronic devices that would not be developed based on conventional materials, such as transistors, sensors, antennas, switching cells, as well as highly promising solar cells, among many other new devices.

Although in this manuscript we focus on graphene's photonic and optoelectronic properties, the inserted subjects can serve as the basis for the study of the technology related to nanophotonic devices based on other two-dimensional (2D) metamaterials that are emerging. For example, black phosphorous (BP) is being highly researched, for the same reason that occurs with graphene, i.e., the very promising electronic, photonic, and mechanical properties.[1] There is a huge interest in 2D silicon – silicene (the term silicene was introduced by Gusmán-Verry and Lew Yan Voon in 2007), due to the preservation of silicon use in the electronic/optical industry, as well as the fact that silicon is the second most abundant chemical element in the earth's crust.[2]

Despite the enormous interest in the use of electromagnetic waves in telecommunications, in the THz frequency range, technologies-based devices related to conventional materials (3D) do not offer conditions to take advantage of this large and important frequency range. On the other hand, materials consisting of one or a few layers of graphene, black phosphorus and transition metal dichalcogenides (TMDs), for example, can be used in optoelectronic devices to operate with electromagnetic waves in this frequency range. It is possible due to their photonic and optoelectronic properties, as well as the possibility of manipulation of the physical parameters inherent to these materials via the application of an external voltage (gate voltage) or chemical doping. In addition, these devices can operate in the modulation-based THz frequency range, nonlinearity, filtering, and plasmonic.[3]

In dense wavelength division multiplexing (DWDM) optical communication networks, the high transmission rate is impaired, because on routers/switches require an optical/electric/optical conversion. Although the fully optical switches already exist for some time, the switching process is poor, since the optical buffers made up of optical delay lines have huge dimensions and difficult operational control. We have obtained a photonic crystal-based optical memory operating similarly to a dynamic random access electronic memory (DRAM).[4] However, we replaced the photonic crystal with graphene, so that we developed a nanophotonic DRAM optical memory with much smaller dimensions and much faster than a DRAM electronic memory, and got its respective patent (INPE/BR 10 2015 029772 6 - 27/11/2015). Besides, due to the nanometric dimensions of the graphene-based devices, we can integrate these referred devices into photonic integrated circuits (PICs), which will replace, with enormous advantages, the current electrical integrated circuits.

It is noteworthy that to work in this area of science, it is necessary to have a thorough knowledge regarding the pho-

*Project partly sponsored by the Cearense Foundation for Scientific and Technological Development Support (FUNCAP) and National Council for Scientific and Technological Development (CNPq).

†Corresponding author. E-mail: awljeng@gmail.com

tonic and optoelectronic properties of graphene. In this review paper, we show the photonic, electrical, and optical properties of graphene in a very well detailed way.

Phonon-plasmon polaritons, exciton-plasmon polaritons and plasmons polaritons are detailed in Section 2. Section 3 is devoted to detailing of the surface plasmons polaritons that occur in graphene (GSPPs). In Sections 4 and 5, we show the optical conductivity and dielectric constant of graphene, respectively. In Section 6, we focus on the dispersion relations for a single graphene layer embedded in a dielectric medium, as well as for two layers separated by a short distance. We have detailed the wavelength vectors and propagation distances of the GSPPs modes in Section 7. The SiO_2 and h-BN substrates, on which graphene is supported, are shown in Section 8. In Section 9, we detail graphene absorbance, transmittance, and reflectance. Finally, Section 10 is dedicated to the application of gate voltage on graphene, through which it is possible to control the level of doping of charges in graphene and consequently its electrical and optical properties.

2. Phonon-plasmon polaritons, exciton-plasmon polaritons, and plasmon polaritons

For a better understanding of the surface plasmon polaritons in graphene (Section 3), we have found it convenient to show first what are phonon-plasmon polaritons, excitons-plasmon polaritons and plasmon polaritons, highlighting the surface phonon-plasmon polaritons, surface excitons-plasmon polaritons, and surface plasmon polaritons.

This subject may be extended to other actively researched 2D materials such as hexagonal boron nitride (insulator),[5] phosphorene (direct bandgap semiconductor),[6] silicene, germanene, and stanene (monolayers of silicon, germanium, and tin, respectively, which are also in the so-called carbon group),[7] and transition metal dichalcogenides (DTMs), i.e., MX_2 (M is a transition metal and X a chalcogen),[8] which are also very promising 2D materials, for the next generation of electronic and optoelectronic devices.

The term polariton is used to represent the tight coupling of an electromagnetic wave with an excited state having a dipole moment (phonon, exciton, or photon). Briefly, for the longitudinal polaritons, the electric field has a nonzero component in the propagation direction. On the other hand, for the transverse polaritons, the electric field has no component in the propagation direction.

Phonon polaritons were first studied by Kun Huang (1951) when he studied photon coupling with the phonon and named this phenomenon as phonon polariton. Following this, in 1958, Hopfield, after researching photon coupling with exciton, defined this coupling as exciton polariton. The theory involving these two phenomena continues being developed to date (bulk and surface). However, concerning plasmons polaritons in graphene (and in other 2D materials), researchers have focused on surface plasmons polaritons.

2.1. Surface phonon-plasmon polaritons

Phonon-plasmon polaritons are quasiparticles that result from strong interactions between photons and phonons, which can occur as surface and volume confined waves. The dispersion relation for phonon polaritons is highly dependent on the material. While volume polaritons tend to approach asymptotically to the longitudinal optical phonon frequency of the material, the surface polaritons tend to approach the surface phonon frequency.[9]

One reason for interest in recent research on bulk and surface polaritons is to obtain optoelectronic devices that operate with electromagnetic waves in the THz and mid-infrared (MIR) ranges.[10–12] We will comment on the results of studies on surface plasmon-phonon polaritons (SPPPs) in doped GaAs, which resulted in the emission of radiation in the THz range.[13]

It is noteworthy that SPPPs occur at the interface of two media with dielectric permittivities of different signs. The dispersion relation for SPPPs is given by[14]

$$k_{\mathrm{SPPP}}^2 = \left(\frac{w}{c}\right)^2 \frac{\varepsilon_1(w)\varepsilon_2}{\varepsilon_1(w)+\varepsilon_2}, \tag{1}$$

where k_{SPPP} is the surface plasmon-phonon polariton wave vector, w is the angular frequency, c is the speed of light, $\varepsilon_1(w)$ is the dielectric permittivity of the first medium (n-doped GaAs in this case), ε_2 is the dielectric permittivity of the second medium (vacuum in this case). For the same frequency (w), the SPPP wave vector is larger than the photon wave vector, and the SPPPs located on the interface can be considered as non-radiative modes. However, SPPPs can be transformed into photons (and vice versa). For this to occur, a regular surface grating should be used in order to reach the phase-matching condition for SPPP and photon[1] (and references therein), i.e.,

$$k_{\mathrm{SPPP}} = k_{\mathrm{Ph}} \sin\theta + mk_{\mathrm{G}}, \quad m = \pm 1, \pm 2, \pm 3, \ldots, \tag{2}$$

with $k_{\mathrm{Ph}} = w/c$ being the wave vector of photon in vacuum, θ the incidence angle, $k_{\mathrm{G}} = 2\pi/a$ the reciprocal vector of the grating, and a the grating period.

Other research has revealed that the electrical permittivity for electron-doped GaAs (n-GaAs), considering the contributions of the lattice, as well as the free electrons, is given by[15]

$$\varepsilon_1(w) = \varepsilon_\infty + \frac{\varepsilon_0 - \varepsilon_\infty}{1 - \left(\frac{w}{w_{\mathrm{TO}}}\right)^2 - \frac{\mathrm{i}w\gamma}{w_{\mathrm{TO}}^2}} - \frac{\varepsilon_\infty w_{\mathrm{p}}^2}{w^2 + \mathrm{i}w\tau^{-1}}. \tag{3}$$

Here, ε_∞ is the high frequency permittivity, ε_0 the low frequency permittivity, w_{TO} the transverse optical phonon frequency, γ the damping constant for the transverse optical phonon, $w_{\mathrm{p}} = \sqrt{\frac{4\pi q^2 N_{\mathrm{e}}}{\varepsilon_\infty m_{\mathrm{e}}}}$ (where N_{e} is the free electron concentration, q is the elementary charge, and m_{e} is the electron effective mass) the plasma frequency, and $\tau = \mu m_{\mathrm{e}}/q$ (where μ is the mobility) the electron relaxation time.

For the existence of surface plasmon-photon polaritons at the GaAs/vacuum interface, it is necessary that $\mathrm{Re}(\varepsilon_1) < 0$, and $|\mathrm{Re}(\varepsilon_1)| > 1$, the curves referring to the real and imaginary parts of ε_1 are plotted as a function of the energy of the modes (in meV) present in a GaAs/vacuum plane interface (Fig. 1).[13]

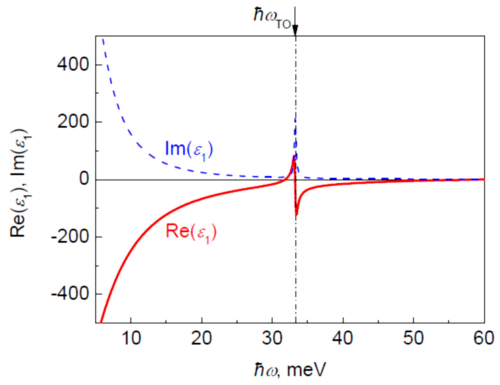

Fig. 1. Real (solid line) and imaginary (dashed line) parts of n-GaAs dielectric permittivity (from Ref. [13]).

It is noteworthy that the following values were considered: the free electron concentration $N_e = 2 \times 10^{18}$ cm^{-3}, and mobility $\mu = 2500$ cm^2/V·s. Moreover, as the GaAs conduction band is nonparabolic, the dependencies of μ and γ on the doping level were taken into account,[16,17] as well as the electron concentration dependence on m_e.[17]

As we can see in Fig 1, for $\mathrm{Re}(\varepsilon_1(\omega)) < -1$, the n-GaAs SPPPs can occur in the ranges between 0 meV and 31.7 meV, and 33.2 meV and 56.9 meV, i.e., for these two energy ranges, there may be surface plasmon-phonon polariton at the n-GaAs/vacuum interface.[13]

From Eqs. (1) and (3) we find the dispersion ratio (SPPP mode energy versus K_{SPPP}, or versus $k_{Ph}\sin\theta + mk_G$, as shown in Fig. 2(a)[13]) for $\theta = 11°$ (solid thick line) and for normal incidence ($\theta = 0°$, Fig. 2(b) solid thick line, adapted from Ref. [13]).

Notice in Fig. 2(a) that the SPPP dispersion relation is made up of two branches, which are separated by a narrow gap. It occurs because the real part of the GaAs permittivity exceeds the value -1, close to the transverse optical phonon energy so that for this energy range, there can be no plasmon-phonon polaritons. The dashed lines shown in this figure indicate the coordinates of the points where there is resonance for different values of m, considering the incident angle $\theta = 11°$.

Figure 2(b) shows the same results for the normal incidence angle ($\theta = 0°$).

The reflectivity that occurs on a flat GaAs/vacuum interface was also investigated, as shown in Fig. 3(a) (adapted from Ref. [13]). As we can see, there are two distinct dips (due to bulk plasmon-phonon polariton excitations).[18]

The insertion of a regular grating at the semiconductor surface (for instance, using photolithography technique) may cause changes in the reflectivity spectrum, which may provide the conversion of photons into surface plasmon-phonon polaritons, as well as the conversion of surface plasmon-phonon polaritons into photons. It is noteworthy that the occurrence of such a conversion may lead to the emergence of resonant dips in the reflectivity spectrum.

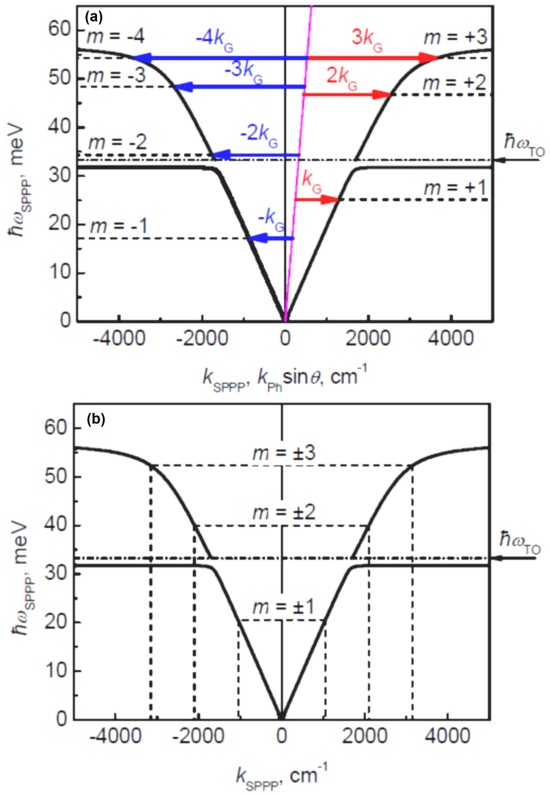

Fig. 2. (a) SPPP mode energy versus K_{SPPP}, or versus $k_{Ph}\sin\theta + mk_G$ for $\theta = 11°$ (solid line). (b) Those for normal incidence (adapted from Ref. [13]).

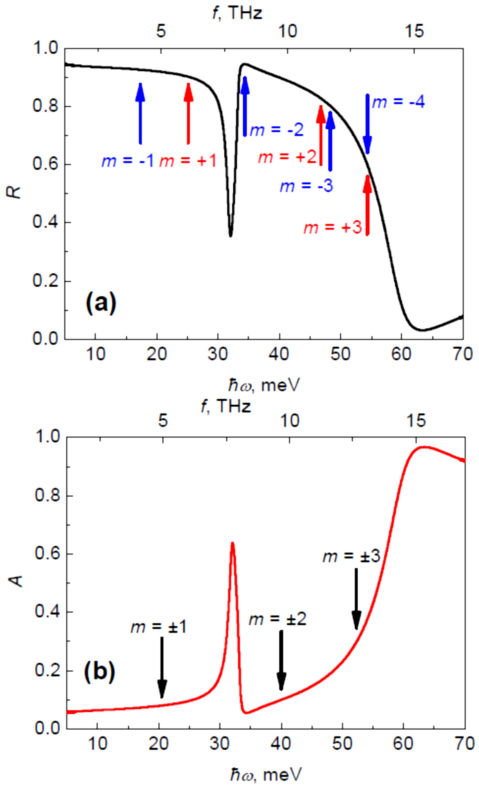

Fig. 3. (a) Reflectivity spectrum in a sem-infinite plane interface GaAs/vacuum. (b) Absorptivity spectrum in a sem-infinite plane interface GaAs/vacuum (adapted from Ref. [13]).

The reflectivity spectrum points were determined (where these dips exist, i.e., SPPP modes excitation occurs), considering the surface grating period $a = 60$ μm, as shown in Fig. 3(a) (arrows), using Eqs. (1) and (2). In these surveys, the absorptivity spectrum of a GaAs semi-infinite surface (plane surface) was also determined, considering the normal incidence of radiation, as shown in Fig. 3(b).

Inserting a surface grating can also alter the absorptivity spectrum of GaAs significantly. It is noteworthy that in this case, as the non-equilibrium SPPPs modes can scatter on the surface grating, there may be the occurrence of a transformation of surface plasmon-phonon polaritons into photons. Consequently, this transformation can cause resonant peaks in the absorptivity spectrum, which are shown in Fig. 3(b), by arrows (obtained via Eqs. (1) and (2), for $a = 60$ μm). Therefore, according to Kirchhoff's law, photon emission in the THz and MIR frequency ranges is expected to occur at the resonant frequencies (where transformations of the surface plasmon-phonon polaritons to photons in n-GaAs occur).

2.2. Excitons-plasmons polaritons

The incidence of photons on the surface of a solid may lead to the occurrence of electron (in the conduction band)–hole (in the valence band) pairs, i.e., excitons, due to the absorption of photons.[19,20] There are two types of excitons: Wanner[21] and Frenkel.[22] Wanner excitons are generally present in semiconductor materials, have weak coupling interaction and wide distributions of electrons and holes. On the other hand, the Frenkel excitons are usually located in insulating materials, have strong Coulomb interaction, and the electrons and holes are bound in somatic cells. Indeed, the incidence of photons in a two-level system (for example, an atom or ion characterized by a ground state and an excited state) can cause the periodic exchange of energy between the light field and this two-level system. The oscillations arising from the above mentioned process, called Rabi oscillations (named after Nobel Prize laureate Isidor Isaac Rabi), are associated with oscillations of electrons and photons. In other words, these oscillations can be defined as a periodic change between absorption and stimulated emission of photons and can be modeled by the Bloch vector formalism. The angular frequency of the Rabbi oscillations is called the Rabi frequency.

The coupling between photon and exciton (exciton-polariton) can be detailed from Maxwell's equations so that the equation that determines the dispersion relationship for excitons-polaritons is given by[23]

$$w^2 = \frac{1}{2\varepsilon_\infty}\left[c^2k^2 + \varepsilon_\infty w_{\mathrm{L}}^2 \pm \sqrt{\left(c^2k^2 + \varepsilon_\infty w_{\mathrm{L}}^2\right)^2 - 4\varepsilon_\infty c^2k^2w_{\mathrm{T}}^2}\right], \quad (4)$$

where k is the wave vector, w_{L} the resonance frequency of the longitudinal mode, and w_{T} the resonance frequency of the transverse mode.

The dispersion relationship for bulk exciton-plasmon polaritons, related to the GaP, is shown in Fig. 4(a) (solid lines) (adapted from Ref. [23]).

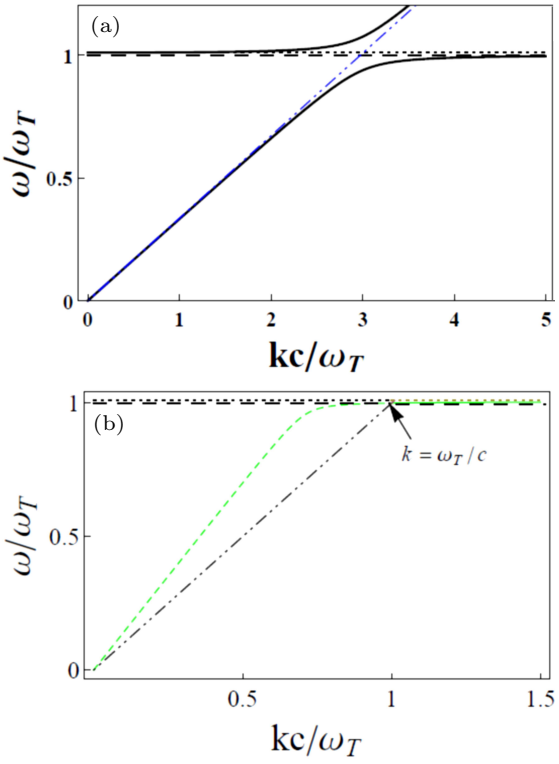

Fig. 4. (a) Dispersion relation of bulk exciton-plasmon polariton in ZnO (solid lines). (b) Dispersion relation of surface exciton-plasmon polariton in ZnO (solid line between w_{T} and w_{L}, adapted from Ref. [23]).

The horizontal dashed line represents the longitudinal resonance frequency, and the dashed-dotted line represents the transverse resonance frequency. Note that there are two branches, upper and lower branches. The longitudinal-transverse splitting, i.e., $w_{\mathrm{LT}} = w_{\mathrm{L}} - w_{\mathrm{T}}$, represents the possibility of coupling strength between the exciton and photon.

The surface exciton-plasmon polariton is made up of strong coupling between photons and excitons, and these modes have the wave vector component in the surface plane. From Maxwell's equations, considering the continuity of the electric field at the surface, it is possible to obtain the dispersion relation of the surface exciton-plasmon polaritons according to the equations shown below:

$$\varepsilon(w)\sqrt{k^2 - \left(\frac{w}{c}\right)^2} = -\sqrt{k^2 - \varepsilon(w)\left(\frac{w}{c}\right)^2}, \quad (5)$$

$$w = ck\sqrt{\frac{1-\varepsilon(w)}{\varepsilon(w)}}, \quad (6)$$

with $\varepsilon(w) = \varepsilon_\infty \frac{w_{\mathrm{L}}^2 - w^2}{w_{\mathrm{T}}^2 - w^2}$ being the dielectric function of the material.[23]

Equations (5) and (6) determine that $\varepsilon < -1$, so that for the existence of surface exciton-plasmon polariton, it is necessary that $w_{\mathrm{T}} < w < w_{\mathrm{L}}$, as shown in Fig. 4(b) (the solid line between w_{T} and w_{L}).

It is noteworthy that both phonon-polariton and exciton-polariton have longitudinal-transverse splitting, i.e., longitudinal-transverse symmetry breaking. However, the LT-splitting for exciton-polariton is small. Note that $w_{\mathrm{LT}} =$ 008 meV for GaAs,[24] and $w_{\mathrm{LT}} = 5.00$ meV for ZnO so that the dispersion relation for the surface exciton-plasmon polariton is approximately linear. Therefore, the effective mass of exciton-polariton approaches infinity, which means that it can not move, and the states in this band can be neglected.

The interaction between localized surface plasmons (LSPs) and photons may provide some advantages regarding optical properties, such as, a longer lifetime of excitons and a large increase in the quantum yield.[25,26] Taking into account that in metal nanostructures can have an energy of localized EM field, the intensity of the electric field can be increased,[27] and there may be nonlinear effects.[28] To achieve a composite structure with enhanced optical properties, hybrid metal/semiconductor structures are being much researched, because of the interaction between SPs and excitons.[29–31]

The combination of metal and semiconductor constituting a hybrid structure provides optical properties which can be used for the nanometer scale of electromagnetic energy flow control. For example, interactions in hybrid structures can be obtained between quantum-confined electronic states located in the semiconductor and confined electromagnetic modes located in the metal. In other words, exciton-plasmon interactions obtained in this way can provide various effects, such as absorption and emission, control of nanoscale energy-transfer processes, creation of new excitations in the strong coupling regime, and increase of optical nonlinearities.[32]

2.3. Surface plasmon polaritons

Surface plasmon polaritons (SPPs) can occur due to the coupling between the oscillations of the electron plasma with photons, which propagate at the interface between a dielectric and a conductor.

To enable the detailing of SSPs in graphene (GSPPs) as well as in other 2D materials, we start from the theory that involves SPPs in metallic interfaces.

From the Maxwell and Helmholtz equations, we can determine the equations that represent the behavior of the metal/dielectric interface SPPs, referring to both sides of this interface, as shown in Fig. 5.

The following equations can be used for TM modes:[14]

$z > 0$:

$$E_x(z) = \mathrm{i}A_2 \frac{1}{w\varepsilon_0\varepsilon_2} k_2 \mathrm{e}^{\mathrm{i}\beta x} \mathrm{e}^{-k_2 z}, \tag{7}$$

$$E_z(z) = -A_2 \frac{\beta}{w\varepsilon_0\varepsilon_2} \mathrm{e}^{\mathrm{i}\beta x} \mathrm{e}^{-k_2 z}, \tag{8}$$

$$H_y(z) = A_2 \mathrm{e}^{\mathrm{i}\beta x} \mathrm{e}^{-k_2 z}, \tag{9}$$

$z < 0$:

$$E_x(z) = -\mathrm{i}A_1 \frac{1}{w\varepsilon_0\varepsilon_1} k_1 \mathrm{e}^{\mathrm{i}\beta x} \mathrm{e}^{k_1 z}, \tag{10}$$

$$E_z(z) = -A_1 \frac{\beta}{w\varepsilon_0\varepsilon_1} \mathrm{e}^{\mathrm{i}\beta x} e^{k_1 z}, \tag{11}$$

$$H_y(z) = A_1 \mathrm{e}^{\mathrm{i}\beta x} \mathrm{e}^{-k_1 z}. \tag{12}$$

Here, $k_{i,z} \equiv k_i$ $(i = 1,2)$ is the component of the wave vector in the direction perpendicular to the interface between the two media, and $\beta(k_x)$ is often referred to as the propagation constant. It is noteworthy that the inverse of the wave vector determines the decay length of the fields in the direction perpendicular to the interface, and consequently, the wave confinement is given by $E_z = 1/\mathrm{e}^{|k_z||z|}$.

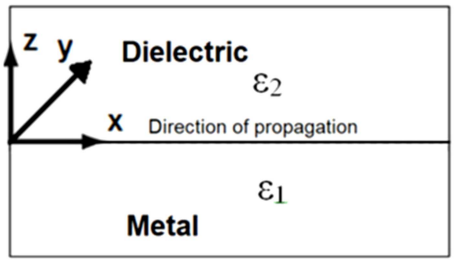

Fig. 5. Schematic representation of an electromagnetic wave propagating in the x-direction of a metal/dielectric planar interface.

Recall that a metal (in this case located at $z < 0$) has a negative real part dielectric function ($\mathrm{Re}[\varepsilon_1(w)] < 0$) for frequencies below the plasmon frequency (w_{p}), and the dielectric (in this case located at $z > 0$) has positive dielectric constant ε_2.

The continuity condition of H_y ad $\varepsilon_i E_z$ at the interface requires that $A_1 = A_2$ so that

$$\frac{k_2}{k_1} = -\frac{\varepsilon_2}{\varepsilon_1}. \tag{13}$$

From Eqs. (7)–(12), we can state that due to the exponent signals adopted in these equations, the confinement of the interface modes requires that the real part of the metal-dielectric constant is negative ($\mathrm{Re}(\varepsilon_1) < 0$), and the dielectric constant of the dielectric is positive ($\varepsilon_2 > 0$). Therefore, surface waves at the metal/dielectric interface can only exist when the materials that make up the interface have the real parts of their dielectric constants with opposite signals, i.e., the interface materials are a conductor and a dielectric. We must state that for the H_y equations related to TM modes (Eqs. (9) and (12)) to comply with the conditions of the wave equation, it is necessary that

$$k_1^2 = \beta^2 - k_0^2\varepsilon_1, \tag{14}$$

$$k_2^2 = \beta^2 - k_0^2\varepsilon_2. \tag{15}$$

On the other hand, from Eqs. (13)–(15), we can arrive at the important expression for the dispersion relation of TM SPP modes that propagate at the interface, given by

$$\beta = k_0 \sqrt{\frac{\varepsilon_1 \varepsilon_2}{\varepsilon_1 + \varepsilon_2}}. \tag{16}$$

Note that equation (16) can be applied to real and complex values of ε_1, that is, for propagating signals in conductors with or without attenuation. On the other hand, for TE modes, we can state that

$z > 0$:

$$H_x(z) = -\mathrm{i}A_2 \frac{1}{w\mu_0} k_2 \mathrm{e}^{\mathrm{i}\beta x} \mathrm{e}^{-k_2 z}, \tag{17}$$

$$H_z(z) = A_2 \frac{\beta}{w\mu_0} \mathrm{e}^{\mathrm{i}\beta x} \mathrm{e}^{-k_2 z}, \tag{18}$$

$$E_y(z) = A_2 \mathrm{e}^{\mathrm{i}\beta x} \mathrm{e}^{-k_2 z}, \tag{19}$$

$z < 0$:

$$H_x(z) = \mathrm{i}A_1 \frac{1}{w\mu_0} k_1 \mathrm{e}^{\mathrm{i}\beta x} \mathrm{e}^{k_1 z}, \tag{20}$$

$$H_z(z) = A_1 \frac{\beta}{w\mu_0} \mathrm{e}^{\mathrm{i}\beta x} \mathrm{e}^{k_1 z}, \tag{21}$$

$$E_y(z) = A_1 \mathrm{e}^{\mathrm{i}\beta x} \mathrm{e}^{k_1 z}. \tag{22}$$

Due to the continuity condition of E_y and H_x in the interface, we have

$$A_1 (k_1 + k_2) = 0. \tag{23}$$

Therefore, for the existence of TE modes in a metal/dielectric interface, it is necessary that $\mathrm{Re}[k_1] > 0$ and $\mathrm{Re}[k_2] > 0$. Hence, we can conclude that to have TE SPP modes on this interface, it is needed that $A_1 = A_2 = 0$, i.e., there are no TE modes at the metal/dielectric interfaces. However, as will be seen later, in graphene/dielectric interfaces, it is possible to have TE modes (although TE modes suffer greater attenuation than the TM modes).

Getting back to the SPPs TM on metal/dielectric interfaces, we can state that the energy of electric and magnetic fields of SPPs at these interfaces has exponential evanescent decay, as shown in Fig. 6.

We can apply the Drude model by adding the effective parameters w_p (plasmon frequency in eV), γ_bulk (proportional to the reciprocal of the mean free time between electron collisions), and ε_0 (contribution of interband transitions to the polarizability)[33] to determine the dielectric function of the metal, as given by

$$\varepsilon(w) = \varepsilon_0 - \frac{w_\mathrm{p}^2}{w^2 + \gamma_\mathrm{bulk}^2} + \mathrm{i}\frac{w_\mathrm{p}^2 \gamma_\mathrm{bulk}}{w(w^2 + \gamma_\mathrm{bulk}^2)}. \tag{24}$$

However, the parameters w_p, γ_bulk, and ε_0 found in the international scientific literature present different values. Taking into account the values that presented the results closest to those obtained experimentally,[34] we adopted the following values for gold:[35] $w_\mathrm{p} = 9.01$ eV, $\gamma_\mathrm{bulk} = 0.072$ eV, and $\varepsilon_0 = 9.84$.

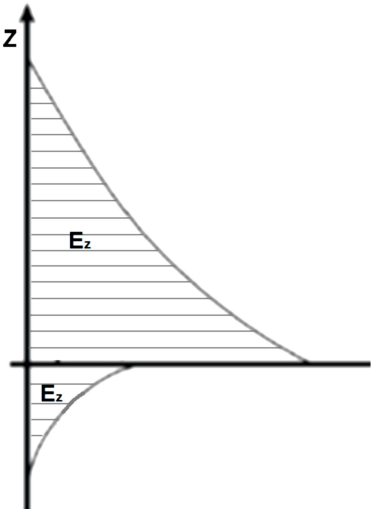

Fig. 6. Schematic representation of evanescent fields in dielectric and metal.

From Eq. (16), we got Fig. 7, by which we can observe the dependence of the real and imaginary parts of the propagation constant as a function of the incident photons energy.

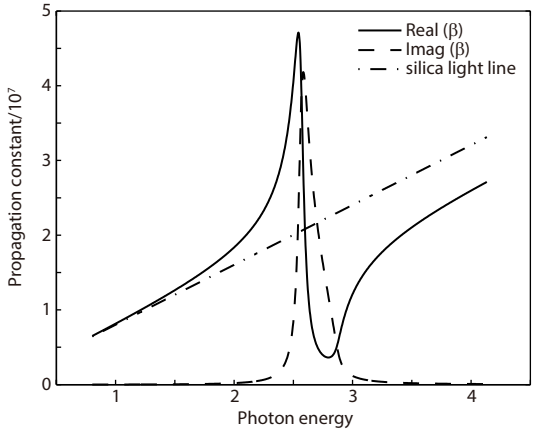

Fig. 7. Real and imaginary parts of the propagation constant of SPPs modes in a gold/silica interface, as a function of the incident photons energy.

We used Eq. (24), adopting the parameters mentioned above, for the determination of the metal dielectric function ε_1, and the dielectric constant of the dielectric (in this case the silica) $\varepsilon_2 = 2.25$.

In Fig. 7, the solid line represents the real part, and the dashed line represents the imaginary part of the SPP modes propagation constant.

Note that we used the energy range between ~ 0.8 eV ($\lambda = 1.55$ μm) and ~ 4.133 eV ($\lambda = 0.3$ μm) for the incident photons, i.e., in the range from infrared to ultraviolet. Interestingly, in this case, the maximum value of the real part for SPP modes is $\beta_\mathrm{m} \approx 4.332 \times 107 + 3.469 \times 107\mathrm{i}$, the energy of this mode is $E_{\beta\mathrm{m}} \approx 2.561$ eV, and $\lambda_{\beta\mathrm{m}} \approx 2\pi/\mathrm{Re}(\beta_\mathrm{m}) \approx$

145.05 nm. It is noteworthy that for values greater than $E_{\beta m}$, the real part of SPPs modes drops dramatically, but from certain energy, the real part of SPPs modes starts to grow again, but less intensely. This means that from this maximum wavenumber value, the value of the wavenumber in the z direction ($k_z = \sqrt{\beta^2 - \varepsilon_2 k_0^2}$) decreases, and consequently, the amount of mode confinement perpendicular to the interface ($E_z = 1/e^{|k_z||z|}$) decreases too. Thus, for energy higher than $E_{\beta m}$, the modes on the interface are no longer SPPs modes and are called quasibound modes.

Besides, for the occurrence of SPPs at the metal/dielectric interfaces, it is necessary to use an insertion technique to achieve the match for the wave vectors of the SPPs and the incident light. Recall that the imaginary part of the propagation constant represents the energy loss of the SPPs modes, that is, the attenuation of the SPPs modes so that the propagation length and wavelength of SPPs modes are given by

$$L_{SPP} = \frac{1}{2\,\mathrm{Im}(\beta)}, \quad \lambda_{SPP} = \frac{2\pi}{\mathrm{Re}(\beta)}. \tag{25}$$

We can still state that SSP modes can be considered as consisting of an electromagnetic wave located in the dielectric, with ($E_{z2} = E_z = 1/e^{|k_{z2}||z|}$) and in metal ($E_{z1} = E_z = 1/e^{|k_{z1}||z|}$).[14] Hence, as $|k_1| \gg |k_2|$, we can conclude that the amount of mode confinement in metal is much smaller than in the dielectric.

3. Graphene surface plasmons polaritons

Although the surface plasmons polaritons in metals (SPPs) and in graphene (GSPPs) come from identical processes, their physical characteristics are different. The main reason for this occurrence is because, in graphene, the electrons are practically free in the normal direction to the plane. It is noteworthy that in graphene, electrons behave like massless Dirac fermions, which gives excellent properties, such as charge carriers (electrons and holes) with high mobility and relatively long average propagation length. Moreover, graphene provides the charge density management via gate voltage (or chemical doping), as well as anomalous Hall effects, among many other advantages, compared to noble metals.[36,37]

The aforementioned, combined with the different dispersion relations, provide different TM modes in graphene (compared to what happens in metals), which brings other advantages, such as higher concentrations of fields, electric and magnetic, as well as higher wavelengths ratio from photons in air and surface plasmons polaritons ($\lambda_{air}/\lambda_{GSPP}$), as well as higher propagation length of GSPPs. Note that this last cited advantage provides much more efficient graphene-guided nanophotonic devices based on guided waves. Besides, in graphene, TE modes can be coupled, unlike noble metals, which are much more expensive than graphene.

We can also cite the fact that due to the physical properties of GSPPs, graphene can enhance photon absorption.[38,39] Incident light can be completely absorbed in nano-disks with graphene matrix structures, depending on the angle of the incident light.[40]

As we will detail in the following sections, the electrical and optical properties of graphene are based on plasmon. We can note that these properties are being increasingly researched, resulting in new and efficient optoelectronic devices. Research has been conducted to investigate the coupling process of radiations emitted by an emitter located above and adjacent (in the same plane) to the plane of a thin graphene film with SPs modes present.[41] Radiations have been polarized in all three dimensions to find out which type of emission is the most efficient. An emitter is located 30 nm above the graphene plane so that the emitted radiation reaches the central part of the plane. When the emitted radiation has polarization in the y-direction, the coupling efficiency between the emitted radiation and the GSPPs rises (greater amount of transmitted energy, i.e., more GSPPs modes are produced). The coupling efficiency for the polarization of the light in the y-direction is greater than that polarized in x and z-directions (z-direction is normal to the graphene plane). On the other hand, when the light emitter is located on the same plane as the graphene film, it is obvious that there is no coupling when the radiation is polarized in the z-direction. Moreover, the coupling efficiency for the x and y-directions is lower than that for the light emitter located above this plane. Hence, unlike metal/dielectric interfaces, where it is necessary to apply a Kretschmann or an Otto configuration to enable the coupling of photons to SPPs, in graphene, photons can be directly coupled to GSPPs.

Hybrid structures based on graphene and other 2D and 3D materials are providing excellent results. A photodetector consisting of a multilayer MoS_2 thin film and a thin layer of graphene quantum dots over the MoS_2 layer was presented, which has photo responsiveness of approximately 10^4 A·W^{-1} and a photo gain of approximately 10^7 electrons per photon. This phenomenon is caused due to the effective transfer of charge and re-absorption of photons during the photons incidence. Thus, the light–matter interaction is enhanced, causing enhanced light absorption as well as the creation of electron–hole pairs.[42]

In the following sections, we will detail the GSPPs-based electrical and optical properties of graphene.

4. Optical conductivity of graphene

Even considering the ideal graphene, i.e., without charge density at Dirac point, its conductivity is not null, since graphene has a universal conductivity (for any frequency) with

value $\sigma_0 = \frac{e^2}{4\hbar} \approx 6.084 \times 10^{-5}\ \Omega^{-1}$, according to the massless Dirac fermion model, in 2D systems.[43,44]

However, it is possible to move the Fermi level (E_F) located at the Dirac point up (electrons (n)-doped)) or down (holes (p)-doped)) by applying a gate voltage, or a chemical doping, so that the change in charge density provides the change of the conductivity of graphene.

In the left part of Fig. 8, we show the schematic representation of the intrinsic graphene energy band diagram at the temperature $T = 0$ K, through which we can observe that the Fermi level is located at the Dirac point. Note that in this case, graphene has universal conductivity.

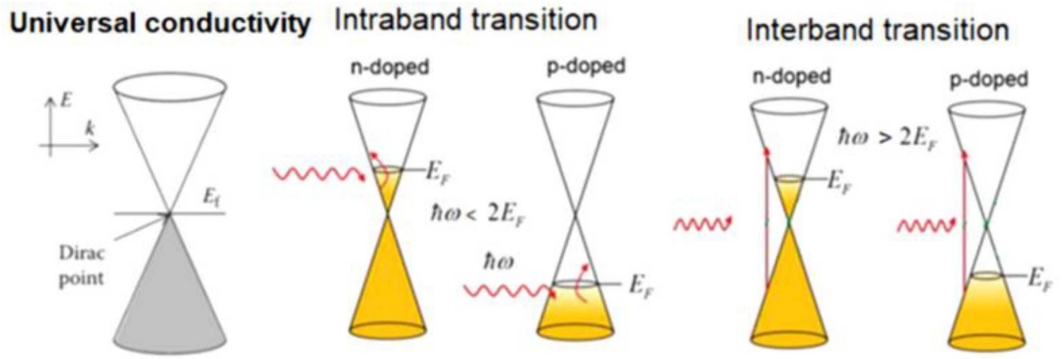

Fig. 8. Schematic representation of the energy band referring to intrinsic graphene (left part), intraband transition (central part), and interband transition (right part).

Note in the central and right parts of Fig. 8 that due to photon absorption, intraband transitions may occur within the conduction (n-doped) and valence (p-doped) bands, as well as interband transitions (between the valence and conductions bands). As we can see, for an interband transition to occur, the photon energy must be greater than twice the Fermi level. On the other hand, i.e., for the occurrence of intraband transition, the photon energy must be less than twice the Fermi level, as it will be further detailed in this section.

In addition to what we have shown above, to detail graphene conductivity, it is also necessary to show the relationship of the chemical potential (μ) with the Fermi level, as well as the equations that determine the chemical potential, charge density (n), and electron relaxation time (τ) for graphene. Therefore, considering the value of the $K_B T/\mu$ ratio too small, we can state that[44–47]

$$\mu \approx E_F \left[1 - \frac{\pi}{12}\left(\frac{K_B T}{\mu}\right)\right] \approx E_F \approx \hbar V_F \sqrt{n\pi}, \tag{26}$$

$$n = \frac{\mu^2}{\hbar^2}\frac{1}{\pi V_F^2}, \tag{27}$$

$$\tau = \frac{\mu_m \mu}{e V_F^2}, \tag{28}$$

with μ_m being the load mobility in graphene.

To find the graphene conductivity equation, we start from the following equation:[44,48]

$$\sigma = \sigma_{intra} + \sigma_{inter} = \frac{e^2\left(w + i\tau^{-1}\right)}{i\pi\hbar^2} \times \left[\frac{1}{\left(w + i\tau^{-1}\right)^2}\int_0^\infty E\left(\frac{\delta F(E)}{\delta E} - \frac{\delta F(-E)}{\delta E}\right)d\varepsilon - \int_0^\infty \frac{F(-E) - F(E)}{\left(w + i\tau^{-1}\right)^2 - 4\left(\frac{E}{\hbar}\right)^2}dE\right]. \tag{29}$$

Here, $F(E) = \{1 - \exp[(E-\mu)/K_B T]\}^{-1}$, and the total conductivity is given by the sum of the intraband and interband transitions conductivities. Moreover, it is assumed that $\mu \gg K_B T$ at ambient temperature ($T = 300$ K, i.e., $K_B T \approx 26$ meV).

After some mathematical manipulations, we arrive at the mathematical expression that determines the intraband conductivity[44,49]

$$\sigma_{intra}(w,\mu) = \frac{i e^2 \mu}{\left(\omega + i\tau^{-1}\right)\pi\hbar^2}, \tag{30}$$

$$\sigma_{inter}(w,\mu) = \frac{e^2}{4\hbar}\left[1 + \frac{i}{\pi}\ln\frac{\hbar\left(w + i\tau^{-1}\right) - 2\mu}{\hbar\left(w + i\tau^{-1}\right) + 2\mu}\right], \tag{31}$$

where e is the electron charge. Note that for $\mu = 0$, $\sigma_{intra} = 0$ and $\sigma = \sigma_{inter} = \frac{e^2}{4\hbar} = \sigma_0$.

We also rely on the following equation for the determination of graphene conductivity:[50]

$$\frac{\sigma(\Omega)}{\varepsilon_0 c} = 4\alpha\frac{i}{\Omega} + \pi\alpha\left[\vartheta(\Omega - 2) + \frac{i}{\pi}\ln\left|\frac{\Omega - 2}{\Omega + 2}\right|\right], \tag{32}$$

where $\Omega = \hbar w/\mu$ is the normalized frequency (without unit), $\alpha = e^2/4\varepsilon_0\hbar c \approx 1/137$ is called the fine structure constant, and $\vartheta(x)$ is the Heaviside step function.

In the above equations, the conductivity values are given as sheet conductivity (with uniform thickness) in Siemens (S). Briefly, to transform sheet conductivity to volume conductivity (S/m), it is necessary to divide the value of the sheet conductivity by the thickness of the film.

Equations (30)–(32) present identical results, as can be seen from Fig. 9, where the graphs of real part (upper part of Fig. 9) and imaginary part (lower part of Fig. 9) of the isolated graphene are shown as a function of $\Omega = \hbar w/\mu$ (wavelength ranging from 0.2 μm to 1.6 μm), for $\mu = 0.5$ eV (solid line) and $\mu = 1.8$ eV (dashed line).

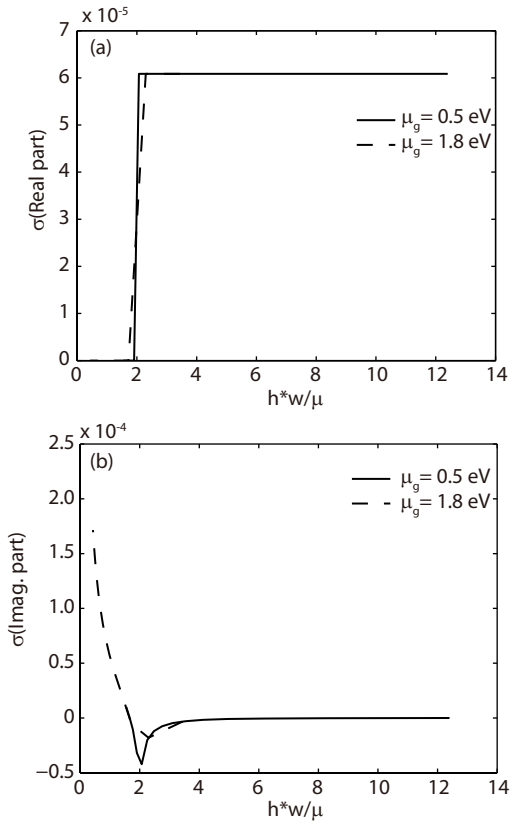

Fig. 9. (a) Real part and (b) imaginary part of the conductivity for a graphene layer (as a function of Ω).

We use the value of load mobility in isolated graphene (3.39×10^5 cm$^2\cdot$V$^{-1}\cdot$s^{-1}).[51] Note at the top of Fig. 9 that for $\Omega=\hbar w/\mu<2$ ($\mu>\hbar w/2$), the real part of graphene conductivity is virtually zero (no interband interactions) and that for $\Omega=\hbar w/\mu>2$ ($\mu<\hbar w/2$), the real part of conductivity has the value of universal conductivity (due to interband interactions).

It is necessary to block interband transitions, i.e., the first-order process, by increasing the graphene's chemical potential to avoid the changing in the conductivity. Thus, only GSPPs with a frequency above the limit ($\hbar w_{\rm inter}/\mu=2\rightarrow w_{\rm inter}=2\mu/\hbar$) suffer this type of attenuation.

However, it has been proven through research that there is still another mechanism of energy loss of SPPs (including GSPPs), which is caused by the phonon emission (second-order process) and the consequent occurrence of electron–hole pair. It is noteworthy that this second-order process, although often neglected, happens for frequencies above a certain threshold ($w_{\rm oph}$), i.e., $w>w_{\rm oph}$ since losses are negligible for frequencies below this threshold. It is important to state that for $w_{\rm oph}<w<w_{\rm inter}$ optical losses, as the first-order process is avoided, but attenuations still occur due to the second-order process. In these researches, the optical loss values were obtained using the methods random-phase approximation (RPA) and number conserving relaxation-time (RT) for the second-order process.[52]

5. Effective relative permittivity

The general equation that gives the effective relative permittivity (dielectric constant) of isolated graphene is given by[53]

$$\varepsilon_{\rm rg}=1+{\rm i}\frac{\sigma}{w\varepsilon_0\Delta},\tag{33}$$

with Δ being the effective thickness of graphene. To facilitate the numerical simulations, we considered $\Delta=0.7$ nm.

However, for the determination of the effective relative permittivity of graphene, another equation was obtained. In this case, by admitting a volume conductivity as a function of very thin thickness, i.e., $\Delta\rightarrow0$ (to recover the two-dimensional geometry of graphene), this equation is given by[54]

$$\varepsilon_{\rm rg}=-\frac{\sigma''}{w\Delta}+\varepsilon_0+{\rm i}\frac{\sigma'}{w\Delta},\tag{34}$$

where σ' and σ'' represent the real and imaginary parts of graphene, respectively.

Note that in this case, the real part of the graphene's effective relative permittivity is given by $\varepsilon'=-\frac{\sigma''}{w\Delta}+\varepsilon_0\approx-\frac{\sigma''}{w\Delta}$ and the imaginary part by $\varepsilon''={\rm i}\frac{\sigma'}{w\Delta}$. Therefore, considering a very thin thickness, the real part of the graphene permittivity can be positive or negative, depending on the imaginary part of the graphene conductivity. Hence, the real part of this permittivity being negative may provide the occurrence of TM modes (($\varepsilon'<0$, $\sigma''>0$)). On the other hand, being positive, it can provide the occurrence of TE modes ($\varepsilon'>0$, $\sigma''<0$). Consequently, TM or TE modes may occur ($\varepsilon'=\varepsilon_0-\frac{\sigma''}{wt}>0$, that is $\sigma''<0$)) in graphene.[54] We will return to this subject in the next section.

Besides, an equation concerning the effective relative permittivity, which takes into account the air impedance ($\eta_0\approx377\ \Omega$), photon wavenumber of the vacuum (k_0), as well as the 2D graphene conductivity (σ) is given by[45]

$$\varepsilon_{\rm rg}=1+\frac{{\rm i}\sigma\eta_0}{k_0\Delta}.\tag{35}$$

6. Dispersion relation

6.1. Single graphene layer embedded in a dielectric medium

The dispersion relationship obtained from Maxwell's equations for TM modes, considering the dielectric layer embedded in two distinct dielectrics, is given by[45]

$$\frac{\varepsilon_{d1}}{\sqrt{\beta_{\rm TM}^2-\varepsilon_d k_0^2}}+\frac{\varepsilon_{d2}}{\sqrt{\beta_{\rm TM}^2-\varepsilon_d k_0^2}}+\frac{{\rm i}\sigma}{w\varepsilon_0}=0,\tag{36}$$

where ε_{d1} and ε_{d2} are the dielectric constants of the dielectric medium, $\beta_{\rm TM}$ is the SSP wavevector (TM mode), k_0 and w are

the wavenumber and angular frequency of the incident photon, and σ is the graphene conductivity. Therefore, from Eq. (36), we can obtain the dispersion relation for TM modes, assuming the graphene sheet embedded in a single dielectric, which is given by[45,46]

$$\beta_{\mathrm{TM}} = k_0 \sqrt{\varepsilon_d - \left(\frac{2\varepsilon_d}{\sigma\eta_0}\right)^2}, \tag{37}$$

with $\eta_0 = \sqrt{\mu_0/\varepsilon_0} \approx 377\ \Omega$ being the intrinsic impedance of free space.

We can state that for TE modes using the same reasoning as above, the dispersion relation for graphene embedded in a dielectric medium is given by

$$\beta_{\mathrm{TE}} = k_0 \sqrt{\varepsilon_d - \left(\frac{\sigma\eta_0}{2\varepsilon_d}\right)^2}. \tag{38}$$

We saw in Section 4 that considering the real and imaginary parts of conductivity ($\sigma = \sigma' + \sigma''$), the effective relative permittivity of graphene is given by $\varepsilon_{\mathrm{rg}} = \varepsilon_0 - \frac{\sigma''}{wt} + \mathrm{i}\frac{\sigma'}{wt}$. Hence, we can get both the real and imaginary parts of the graphene permittivity, which are given by $\varepsilon'_{\mathrm{rg}} = \varepsilon_0 - \frac{\sigma''}{wt}$ and $\varepsilon''_{\mathrm{rg}} = \mathrm{i}\frac{\sigma'}{wt}$, respectively. Therefore, for convenience, repeating what we have shown in Section 3, the real part of the graphene permittivity may be positive or negative, depending on the value of the imaginary part of the graphene conductivity. It is noteworthy that the real part of this permittivity being negative may provide the occurrence of TM modes. On the other hand, being positive can provide the occurrence of TE modes. Consequently, graphene may have TM ($\varepsilon'_{\mathrm{rg}} = \varepsilon_0 - \frac{\sigma''}{wt} < 0$, i.e., $\sigma'' > 0$) or TE modes ($\varepsilon'_{\mathrm{rg}} = \varepsilon_0 - \frac{\sigma''}{wt} > 0$ that is $\sigma'' < 0$).[54]

The plot of the imaginary part of graphene conductivity in air calculated by Eqs. (30) and (31) (dashed line), as well as the graph of the real part of the relative permittivity of graphene (solid line), according to Eqs. (30) and (31), is shown in Fig. 10.

In Fig. 11, we can see in more detail that for TM GSPP mode and TE GSPP mode to be supported on graphene, it is necessary that $0 < \hbar w/\mu_{\mathrm{g}} < 1.667$ ($\sigma'' > 0$) and $1.667 < \hbar w/\mu_{\mathrm{g}} < 2$ ($\sigma'' < 0$), respectively.[55]

Note that for $\hbar w/\mu_{\mathrm{g}} > 2$, the real part of the graphene conductivity is greater than zero so that the TE modes are attenuated, and there are no TE modes.

It is noteworthy that the increase in temperature causes a slight change in the real part of graphene conductivity around the bifurcation point (where $\sigma' = 0$) so that the real part of conductivity becomes slightly positive for some values of $\hbar w/\mu_{\mathrm{g}} \approx< 2$, which results in small attenuations of GSPPs modes. However, TE modes suffer greater attenuation than TM modes.[45]

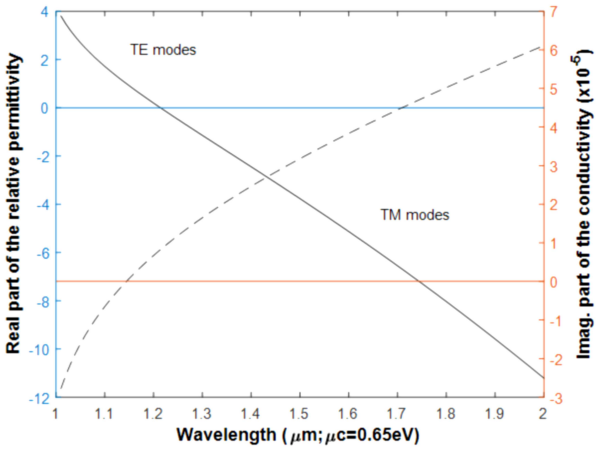

Fig. 10. Real part of graphene's relative permittivity (*y*-axis on the left, solid line) and imaginary part of graphene conductivity (*y*-axis on the right, dashed line) as a function of incident photon wavelength (1 μm < λ < 2 μm), considering $\mu_{\mathrm{c}} = 0.65$ eV).

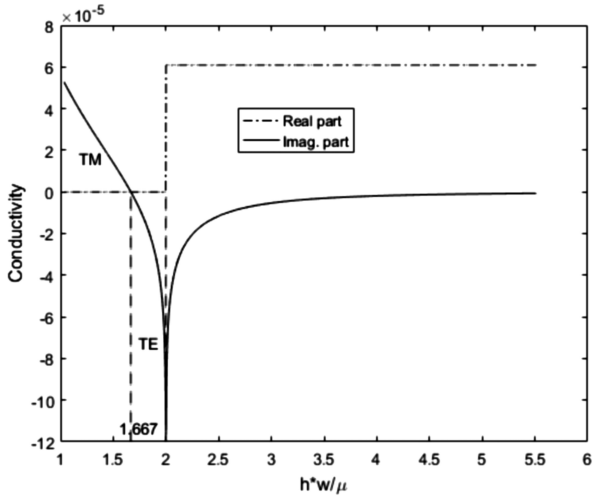

Fig. 11. Graphene conductivity as a function of $\hbar w/\mu_{\mathrm{c}}$.

6.2. Two graphene sheets embedded in a dielectric medium

The schematic representation of a double-layer of graphene, embedded between 3 dielectric media, is shown in Fig. 12(a). We can see the schematic representation of the electric field profile of the hybrid GSPP mode in Fig. 12(b), which is constituted by the overlap of the GSPP modes located in each of the graphene layers.

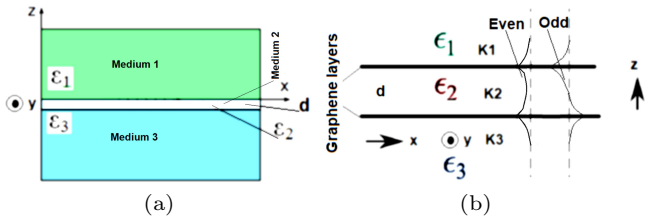

Fig. 12. (a) Schematic representation of a nanophotonic device consisting of two parallel graphene layers embedded in 3 different dielectric media. (b) Schematic of the hybrid field GSPP mode profile.

From the equations that determine the electric fields, applying the boundary conditions on both interfaces, and assuming exponential decay of the fields, we can get the dispersion

relation for this device[56]

$$\begin{aligned} &e^{dk_2}\left(\frac{\varepsilon_1}{k_1}+i\frac{\sigma}{w\varepsilon_0}+\frac{\varepsilon_2}{k_2}\right)\left(\frac{\varepsilon_3}{k_3}+i\frac{\sigma}{w\varepsilon_0}+\frac{\varepsilon_2}{k_2}\right)\\ &=e^{-dk_2}\left(\frac{\varepsilon_1}{k_1}+i\frac{\sigma}{w\varepsilon_0}-\frac{\varepsilon_2}{k_2}\right)\left(\frac{\varepsilon_3}{k_3}+i\frac{\sigma}{w\varepsilon_0}-\frac{\varepsilon_2}{k_2}\right),\\ &k_m^2=\beta^2-\frac{\varepsilon_m w^2}{c^2}. \end{aligned} \tag{39}$$

In the case that medium 1 is equal to medium 3, equation (39) becomes

$$\begin{aligned} &\left[\left(\frac{\varepsilon_1}{k_1}+i\frac{\sigma}{w\varepsilon_0}\right)\cosh\left(\frac{dk_2}{2}\right)+\frac{\varepsilon_2}{k_2}\operatorname{senh}\left(\frac{dk_2}{2}\right)\right]\\ &\times\left[\left(\frac{\varepsilon_1}{k_1}+i\frac{\sigma}{w\varepsilon_0}\right)\operatorname{senh}\left(\frac{dk_2}{2}\right)+\frac{\varepsilon_2}{k_2}\cosh\left(\frac{dk_2}{2}\right)\right]=0. \end{aligned} \tag{40}$$

Indeed, the first term represents the even mode and the second term represents the odd mode.

Assuming all dielectrics are equal, that is, $\varepsilon_1=\varepsilon_2=\varepsilon_3=\varepsilon_d$ and $\beta\gg w\sqrt{\varepsilon_d}/c$ (non-delayed approximation or plasmon approximation), equation (40) reduces to

$$2\varepsilon_d e^{\beta d}+i\frac{\beta\sigma}{w\varepsilon_0}\left(e^{qd}\pm 1\right)=0. \tag{41}$$

It is noteworthy that while the + sign in Eq. (41) represents the dispersion relation for the even mode, the − sign represents the dispersion relation for the odd mode.

On the other hand, according to the conventional waveguide theory, the electric fields in the different regions of the double-layer graphene device (Fig. 13, considering $\varepsilon_1=\varepsilon_2=\varepsilon_3=\varepsilon_d$) can be determined by the following equations:[46]

$$\begin{aligned} &E_z=Ae^{-k_d(z-b)},\quad b<z<\infty,\\ &E_z=Be^{k_g(z-b)}+Ce^{-k_g(z-a)},\quad a<z<b,\\ &E_z=De^{k_d(z-a)}+Ee^{-k_d(z+a)},\quad -a<z<a,\\ &E_z=Fe^{k_g(z+a)}+Ge^{-k_g(z+b)},\quad -b<z<-a,\\ &E_z=He^{k_d(z+b)},\quad -\infty<z<-b, \end{aligned} \tag{42}$$

where $k_d=\sqrt{\beta^2-\varepsilon_d k_0^2}$, $k_g=\sqrt{\beta^2-\varepsilon_{rg}k_0^2}$, β is the propagation constant (wave vector in the propagation direction) of the GSPPs modes, and coefficients $A,\ldots,H$ are the amplitudes of the modes in the different regions.

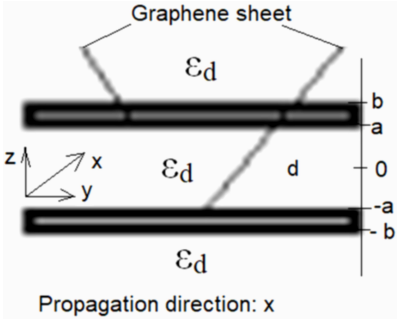

Fig. 13. Schematic representation of the device with two layers spaced apart from one another.

Taking into account the boundary conditions (the transverse electric and magnetic fields are continuous at the interfaces), as well as using the limit for the smallest possible value of the distance d, when $d\to 0$, the dispersion relation of this device is given by

$$-k_d\left(\pm e^{-k_d}-1\right)=\frac{2i\varepsilon_d k_0}{n_0\sigma}. \tag{43}$$

There are two solutions concerning Eq. (43), i.e, the coupled, symmetrical (even, β_{even}), and anti-symmetrical (odd, β_{odd}) modes, which can be roughly determined adopting $\beta_{even}=\beta+\Delta\beta_+$ and $\beta_{odd}=\beta+\Delta\beta_-$, where $\Delta\beta_+$ and $\Delta\beta_-$ represent small amounts with respect to the propagation constant in an isolated graphene sheet (β)[46]

$$\beta_\pm\approx\beta+\frac{2i\varepsilon_d k_0/(\eta_0\sigma)-k_d(1\mp A)}{(1\mp B)\beta/A\pm B\beta d}, \tag{44}$$

where + and − signs represent the symmetric and anti-symmetric modes, respectively, and $k_d=\sqrt{\beta^2-\varepsilon_d k_0^2}$ $eA=e^{-k_d d}$.

We plot the real parts of the even and odd mode propagation constants using Eq. (44) (left y-axis for Fig. 14), considering the same parameters adopted in Ref. [46], i.e., $\lambda_0=10$ μm (wavelength of incident light), $\mu=0.15$ eV (applied to both graphene layers), $\tau=0.5$ ps, 0.02 μm $<d<$ 100 μm, and $\varepsilon_d=1$, in order to compare the results obtained.

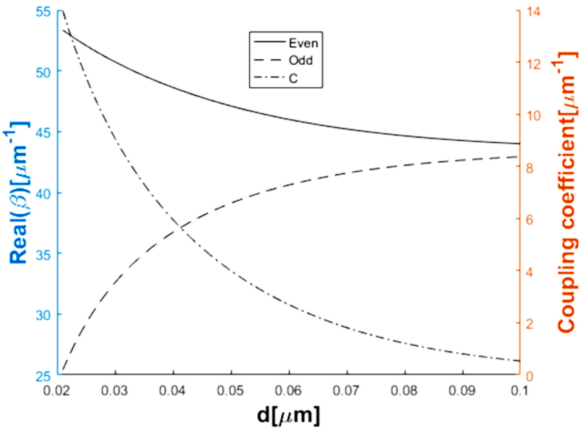

Fig. 14. Graphs referring to dispersion relations for even and odd modes, and coupling coefficient, according to the parameters presented above.

The results are identical, and the slight difference between the values may have been caused by the fact that we used the general graphene conductivity equation ($\sigma=\sigma_{intra}+\sigma_{inter}$) according to Eqs. (30) and (31). Note that the real part values related to the wavenumbers in the propagation direction of the even modes are greater than the real part values of the odd modes. We can also see that for values from 100 nm onwards, the real parts of the propagation constants of the even and odd modes approximate the value of the propagation constant on a single graphene layer.

It is noteworthy that this device can operate as a directional coupler whose coupling coefficient (C) is given by[46]

$$C = \frac{q_{\text{even}} - q_{\text{odd}}}{2}, \tag{45}$$

as we can see in the right-hand axis of Fig. 14.

For comparison, in Fig. 15, we also plot the same parameters determined in Fig. 14, but using $\lambda_0 = 1.55$ μm, $\mu = 0.5$ eV (applied to both graphene layers), and 2 nm $< d <$ 2.5 nm using hexagonal boron nitride (h-BN) as the dielectric. We considered the mobility of graphene $\mu_{\text{m}} = 60000$ cm^2/V·s and the dielectric constant between 3 and 4[57,58]). In Section 8, we will detail the most commonly used substrates to support graphene.

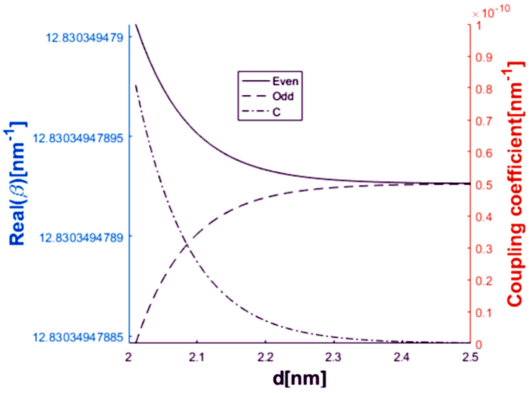

Fig. 15. Graphs of relation dispersions for even and odd modes and coupling coefficient using h-BN as dielectric and the parameters mentioned above.

7. GSPPs wavelengths, wavenumbers, wavelengths ratio, and propagation lengths

Taking into account a graphene sheet over h-BN, according to Eq. (27), if we use, for example, $\mu_{\text{g}} = 05$ eV, we can find that the graphene charge density is $n \approx 1,837 \times 10^{13}$ cm^{-2}, and according to Eq. (28), we have $\tau = 3$ ps. The wavelengths of the GSPP modes, as well as the propagation length (distance traveled by the GSPP mode until its energy decays to 1/e from its initial value), can be determined from their wave vectors[59–61]

$$\lambda_{\text{GSPP}} = \frac{2\pi}{\text{Re}[\beta]}, \tag{46}$$

$$\delta_{\text{GSPP}} = \frac{1}{2\,\text{Im}[\beta]}. \tag{47}$$

To get an idea of the relationship between the wavelength of the radiation before coupling (in the air) and the wavelength of the GSPP mode, we consider, for example, $\lambda_0 =$ 8 μm ($E_{\text{foton}} \approx 0,155$ eV), $\mu = 04$ eV, and mobility $\mu_{\text{m}} =$ 10000 cm^2/V·s for graphene embedded in SiO_2. In this case, we have $\lambda_0/\lambda_{\text{GSPP}} \approx 184$ (obtained from Eqs. (37) and (46)). On the other hand, $\delta_{\text{GSPP}} \approx 266$ nm (obtained from Eqs. (37) and (47)).

It is noteworthy that for the same conditions as above, but using graphene over h-BN, we have $\lambda_0/\lambda_{\text{GSPP}} \approx 165$ and $\delta_{\text{GSPP}} \approx 1775$ μm. Note that the propagation length in graphene over h-BN is approximately 6.673 greater than that in graphene over SiO_2.

Figure 16 plots the real and imaginary parts of the wavenumbers in the propagation direction, considering the wavelengths of the incident photons on a graphene sheet embedded in an h-BN substrate (TM mode) [(a), (b)] ranging from 1 μm to 2 μm, with the chemical potential of graphene $\mu = 0.5$ eV; and [(c), (d)] ranging from 2 μm to 3 μm, with the chemical potential of graphene $\mu = 0.3$ eV.

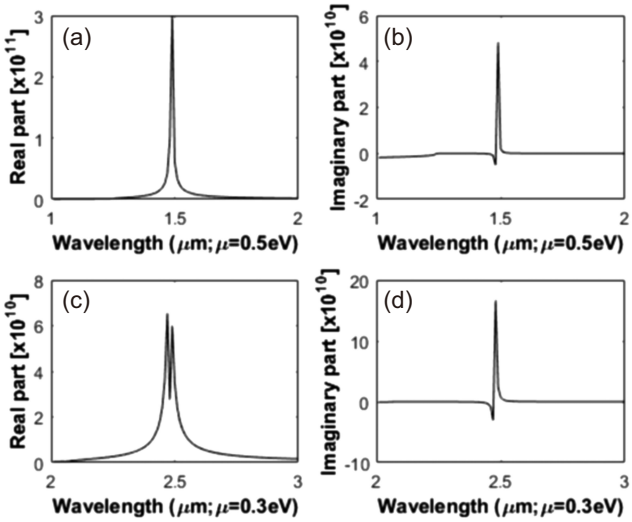

Fig. 16. (a) Real and (b) imaginary parts of GSPP wavelength numbers in the propagation direction for incident photons with wavelengths ranging from 1 μm to 2 μm in a graphene sheet ($\mu = 0.5$ eV) embedded in an h-BN substrate (TM mode). (c), (d) For photons with wavelengths ranging from 2 μm to 3 μm ($\mu = 0.3$ eV).

Figure 17(a) plots the ratios of wavelengths between the photon in the air and the GSPP modes in graphene over h-BN, considering the wavelengths of the photons in the air in the range 1.5 μm $< \lambda_0 <$ 2.0 μm for $\mu = 0.5$ eV and 0.55 eV. Note that for the conditions mentioned above, the higher the chemical potential, the lower the $\lambda_{\text{GSPP}}/\lambda_0$ ratio and obviously, the higher the λ_0, the lower this ratio too.

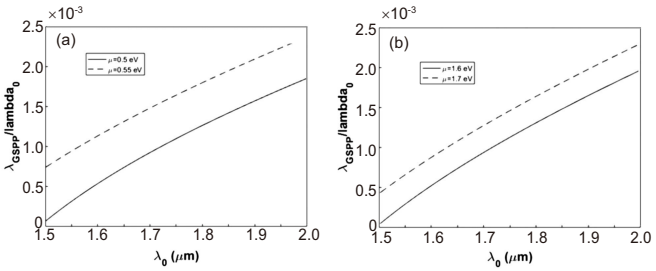

Fig. 17. The $\lambda_{\text{GSPP}}/\lambda_{\text{ar}}$ ratio as a function of λ_0.

Figure 17(b) plots the ratios between GSPP mode wavelengths and air photon wavelengths for air photon wavelengths

in the range 0.5 μm $< \lambda_0 <$ 0.70 μm with $\mu = 1.60$ eV and 1.75 eV.

As we can see (for the conditions mentioned above), the higher the chemical potential, the lower the ratio λ_{GSPP}/λ_0 and, the higher the λ_0, the lower this ratio.

8. SiO_2 and h-BN substrates

The quality of the substrate on which a graphene sheet is deposited needs to be carefully checked to maintain graphene with good quality. This is very important because to obtain graphene with good quality (after its transfer), the substrate must be free of wrinkles, distortion, and other types of defects. However, the thermal deposition of SiO_2 usually causes high surface roughness, and graphene over SiO_2 has no homogeneity of charges along its surface.

For comparison, while a SiO_2 surface with dimensions 0.5 μm × 0.5 μm has R_{pm} (average of the highest roughness peaks above the average level in five measurements) = 250, an h-BN surface with the same dimensions has $R_{pm} = 50$.[62]

A single layer of h-BN, termed white graphene, is also contained in a plane. This material is a graphene isomorphic, in which the boron and nitrogen atoms are located at points A and B of the same atomic structure presented for graphene so that the atomic structure of h-BN is similar to that of graphene. Note that boron and nitrogen atoms are the closest neighbors to carbon atoms in the periodic table, the number of electrons of two carbons is equal to the sum of the number of electrons of boron and nitrogen.

It is noteworthy that graphene has a unit cell consisting of carbon atoms distanced by 0.142 nm, its atomic lattice has a structure parameter with a value of 0.246 nm. On the other hand, h-BN atoms (boron and nitrogen) are 0.144 nm apart, and its structure parameter has a value of 0.25 nm. Moreover, the space between two layers of graphene is 0.355 nm and the space between two layers of cubic h-BN is 0.333 nm.[63] The value of the dielectric constant of h-BN (between 3 and 4) is close to that of SiO_2.[58,59,64,65]

Besides, we have mentioned above, note at the bottom of Fig. 18, that the surface roughness of an h-BN layer is much smaller than that of a SiO_2 layer. Hence, the graphene sheet is much better positioned at an h-BN surface than at a SiO_2 surface. There are several methods for depositing h-BN layers on a SiO_2/Si substrate, for example, the method detailed in Refs. [58,62].

Despite of the existence of a great similarity of graphene with h-BN, while graphene is considered as a null bandgap semiconductor, h-BN is considered as an insulator, whose bandgap is 5.97 eV.[66] Like graphene, in h-BN, the covalent bonds between boron and nitrogen atoms are composed of sp^2 hybrid covalent bonds, which form strong σ bonds in the plane,[67,68] and the layers are supported by weak van der Waals forces. Therefore, both graphene and h-BN have very strong covalent bonds in the plane and weak van der Waals forces between adjacent planes.

Considering that the h-BN roughness is much lower than the SiO_2 roughness, graphene embedded between h-BN layers has much higher charge mobility and homogeneity, when compared to embedded between SiO_2 layers.

It is noteworthy that the charge mobility of graphene over h-BN has been determined, i.e., $\mu_m = 60000$ cm^2/V·s,[58] which is the value we adopted in our work.

On the other hand, a lot of research has been carried out to determine graphene on SiO_2,[69–72] but the value $\mu_m =$ 10000 cm^2/V·s is the most widely reported in the international scientific literature. Note that this value is much lower than that of graphene on h-BN.

Since there are very few charge traps on the h-BN surface, graphene on h-BN has a marked improvement on its electronic properties, when compared to on SiO_2.[64] Experiments have shown that graphene sheets can withstand electrical current density greater than 10^8 A/cm^2, for widths less than 16 nm. The graphene sheets used in these experiments were produced by exfoliation of graphite through adhesive tapes and adhered to an oxidized silicon substrate with an oxide thickness of 300 nm. The breaking current density is related to the resistivity of the graphene sheet, Joule heating being the most likely breaking mechanism.[73] Therefore, as the resistivity of graphene on SiO_2 is higher than that of graphene over h-BN, the breaking current density in graphene over h-BN must be even higher.

In Fig. 18, we show one of the geometries for a graphene/substrate system that we will use in our nanophotonic devices.

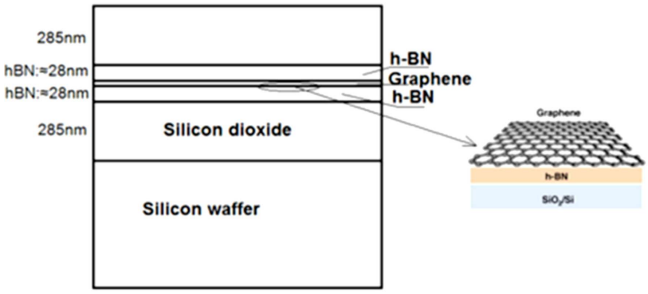

Fig. 18. Schematic representation of a system consisting of a graphene layer embedded between two layers of h-BN.

9. Absorbance, transmittance, and reflectance

As graphene has no prohibited bandgap, the generation of charges due to light absorption occurs over a wide range of

wavelengths, including ultraviolet, visible, infrared, and tera-Hertz ranges, which is not possible by the use of metals. Besides, the transmittance (T) of undoped graphene is independent of the incident photon wavelengths. The T is determined by

$$T = (1-0.5\pi\alpha)^2 \approx 1-\pi\alpha \approx 0.977\ (97.7\%), \quad \alpha = \frac{q^2}{4\pi\varepsilon_0\hbar^2 c}, \tag{48}$$

where α is called the fine structure constant.[43]

On the other hand, a graphene layer has a reflectance of only 0.1% of the incident light. However, for a graphene film constituted by ten layers, this value increases to 2%.[51] Therefore, we can state that a graphene layer has absorbance $A = 1-T \approx 2.3\%$.

Two-dimensional materials such as graphene and MoS_2 have an absorption coefficient $> 5\times10^7$ m^{-1} in the visible light frequency range, which is ten times higher than that of GaAs and Si.[15] Due to its very thin thickness, the absolute value of graphene absorbance is very small. However, the absorbance of some overlapping layers is approximately proportional to the number of these graphene layers.[50–52] On the other hand, this absorbance loses the proportionality mentioned above when it comes to significant graphene layer numbers, but the transmittance remains high. For example, graphene with overlapping layers providing 1 μm thickness has a transmittance of approximately 70%.

The absorption spectrum of a graphene layer is quite flat (between 300 nm and 2500 nm), but there is an absorption peak in the ultraviolet region (≈ 270 nm).[53]

Indeed, absorbance, reflectance, and transmittance depend on some factors, such as materials used above and below the graphene layer, angle of incidence, and type of light polarization. Although we are focusing on graphene, this theory can serve as the base to other 2D group IV materials (silicene, germanene, and tinene).

Graphene embedded in two media ($j = 1,2$), can be characterized by the dielectric functions (or refractive index) of these media. Moreover, the conductivity of graphene defines its effective dielectric constant, which can be complex. We will use the normalized conductivity of graphene ($\sigma_n(w) = \sigma(w)/\varepsilon_0 c = \sqrt{\mu_0}/\varepsilon_0\sigma(w)$).

Let us consider the dielectric functions and the refractive indices of the two media involving the graphene layer, given by

$$\tilde{n}_j(w) = \sqrt{\tilde{\varepsilon}_{rj}(w)} = n_j(w) - ik_j(w), \tag{49}$$

where the real part of the complex refractive index represents the refractive index and the imaginary (negative) part represents the extinction coefficient.

In Fig. 19, we show the schematic representation related to the incidence, reflection, and transmission of light in a medium where graphene is embedded (assuming optical isotropy in the graphene plane (x,y)), considering that the dielectric media where graphene is embedded have null extinction coefficients.

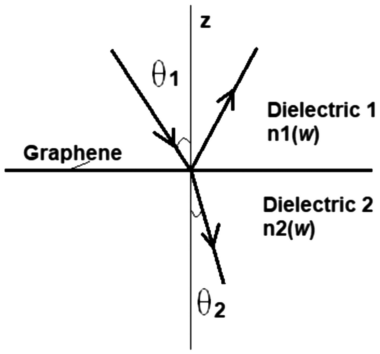

Fig. 19. Light propagating through dielectric graphene junctions, where graphene is embedded in two dielectric media, which have real refractive indices.

However, assuming that the refractive indices of the two media are complex, we have[50,74,75]

$$\tilde{n}_{pj}(w) = \tilde{n}_j(w)\cos\theta_j \text{ (polarization s – TE mode)}, \tag{50}$$

$$\tilde{n}_{pj}(w) = \tilde{n}_j(w)/\cos\theta_j \text{ (polarization p – TM mode)}. \tag{51}$$

It is noteworthy that considering the dielectric medium 1 with real refractive index (with null extinction coefficient), the incidence angle (θ_1) is real and the refractive angle (θ_2) is given by

$$\text{sen}\theta_2 = (n_1/\tilde{n}_2)\text{sen}\theta_1, \quad \cos\theta_2 = \sqrt{1-\text{sen}^2\theta_2}. \tag{52}$$

Note that the refractive angle can be complex. Considering the medium 2 as absorbent, we have the transmittance, reflectance, and absorbance given by[41–43]

$$T = \frac{\tilde{n}_{p2}}{\tilde{n}_{p1}}\frac{4\tilde{n}_{p1}^2}{\left|\tilde{n}_{p1}+\tilde{n}_{p2}+\sigma_n\right|^2}, \tag{53}$$

$$R = \left|\frac{\tilde{n}_{p1}-\tilde{n}_{p2}-\sigma_n}{\tilde{n}_{p1}+\tilde{n}_{p2}+\sigma_n}\right|^2, \tag{54}$$

$$A = 1-(T+R). \tag{55}$$

At the top of Fig. 20 we show the transmittance and reflectance plots of graphene embedded in a single h-BN substrate, whose dielectric constant was considered as $\varepsilon_{hBN} = 3.4$ (real),[22,23,30,31] $\Omega = \hbar w/\mu = 1.8$, and $\mu = 0.5$ eV, ($\lambda \approx 1.378$ μm, TE mode) as well as $\Omega = \hbar w/\mu = 1.5$, and $\mu = 0.5$ eV, ($\lambda \approx 1.653$ μm, TM mode) as a function of the angle of incidence of light (Eqs. (50)–(55)). We have determined the conductivity of graphene according to Eq. (32).

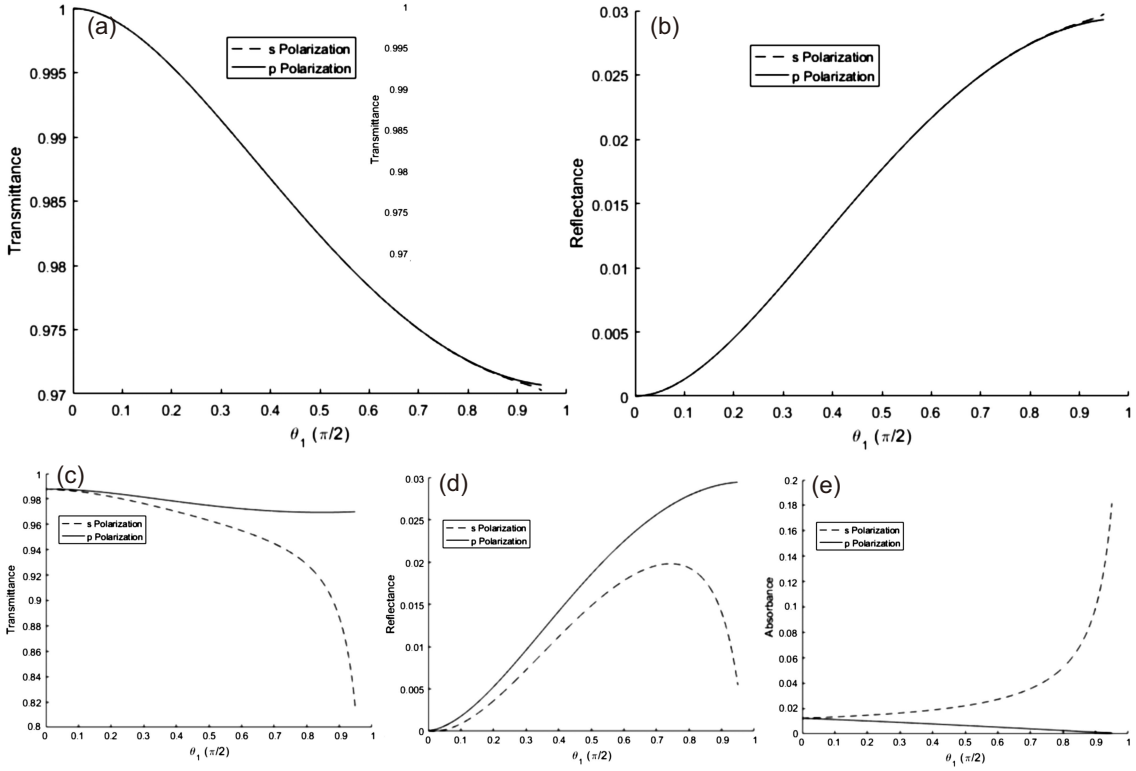

Fig. 20. (a) Transmittance and (b) reflectance graphs for a structure consisting of h-BN/graphene/h-BN as a function of the incidence angle of light, for TM and TE modes without photon absorption. (c)–(e) Graphs of absorbance, reflectance, and absorbance (with photon absorption).

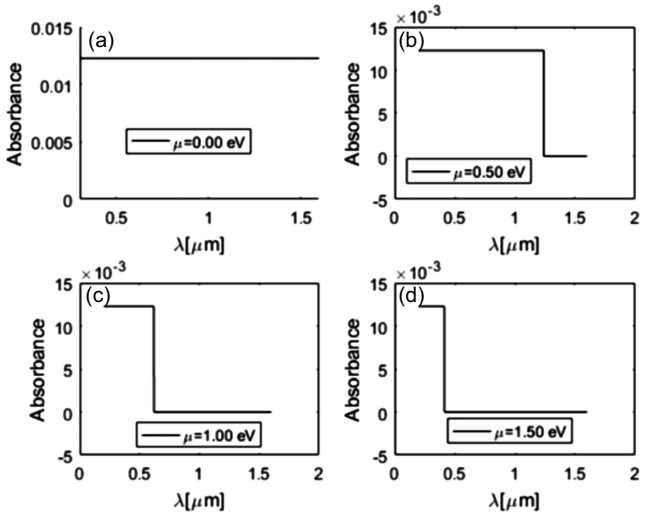

Fig. 21. The absorbances referring to the structure consisting of h-BN/graphene/h-BN as a function of λ, for $\mu = 0.00$ eV, 0.50 eV, 1.00 eV, and 1.5 eV.

Note that in this case, the transmittance and reflectance values for TM and TE modes are about the same. According to that has already been detailed previously, the TM and TE modes do not suffer attenuation (photon absorption).

At the bottom of Fig. 20 we show the transmittance, reflectance, and absorbance plots of a graphene structure embedded in a single h-BN substrate, $\Omega = \hbar w/\mu = 2.5$, and $\mu = 0.5$ eV, ($\lambda \approx 0.992$ μm, TM and TE modes) as a function of the angle of incidence of light. As we can see, in this case, there is an absorption of photons. We can state that while the absorbance for TM modes decreases from approximately 0.02 (normal surface incidence angle) to zero (incidence angle near $\pi/2$ rad), for TE modes it increases from approximately 0.02 to approximately 0.18.

For the same structure mentioned above, we obtained the wavelength absorbance graphs (0.3 μm $\leq \lambda \leq$ 1.6 μm), for $\mu = 0.00$ eV, 0.50 eV, 1.00 eV, and 1.50 eV, considering the normal incidence angle at the surface, as shown in Fig. 21 (for TE and TM modes, whose values in this case coincide).

Note that for $\mu = 0$, all wavelengths are absorbed (universal) since the conductivity is universal. However, for $\mu \neq 0$, from the wavelength that provides $\Omega < 2$, the absorbance value is null. Note that for wavelengths in the range of approximately 0.30 μm to 0.50 μm, photon absorption occurs even at $\mu = 1.5$ eV.

Let us now consider an example of a structure air/graphene/silicon for Schottky junction solar cells. We plot the absorbance and transmittance as a function of the incidence angle for TE and TM modes, considering $\mu = 0$, using Eqs. (45) and (49)–(55), in Fig. 22. The conductivity of graphene has been determined according to Eq. (32) and the dielectric constant of silicon has been considered, with value $\varepsilon_r = 11.7$.

We can conclude that while the transmittance and the absorbance for TE modes decrease as a function of the incidence angle increment, for TM modes, the opposite occurs, with a peak value around the angle 0.45π rad.

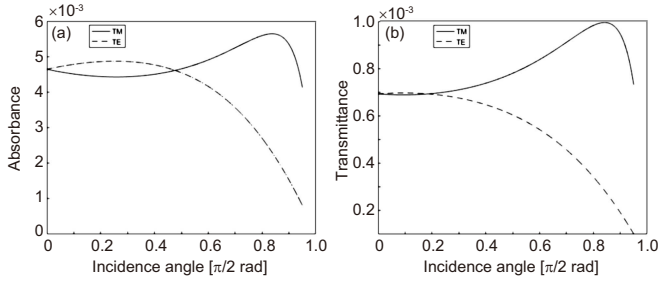

Fig. 22. Graphs of (a) absorbance and (b) transmittance.

In addition to Eq. (55), which is used for determination of the absorbance, we can also use the following equations for TE and TM modes, respectively[50]

$$A_{\mathrm{s}} = \frac{4\sqrt{\varepsilon}_1 \cos(\theta_1)\mathrm{Re}\,(\tilde{\sigma})}{\left(\sqrt{\varepsilon}_1 \cos\,(\theta_1) + \sqrt{\varepsilon}_2 \cos\,(\theta_2) + \tilde{\sigma}\right)^2}, \tag{56}$$

$$A_{\mathrm{p}} = \frac{4\sqrt{\varepsilon}_1 \mathrm{Re}\,(\tilde{\sigma})/\cos(\theta_1)}{\left(\sqrt{\varepsilon}_2/\cos\,(\theta_2) + \left(\sqrt{\varepsilon}_1/\cos\,(\theta_1) + \tilde{\sigma}\right)^2\right.}. \tag{57}$$

However, by analyzing these three equations, we can see that they are the same equations so that the results are the same.

The electrical and optical properties of graphene and other 2D materials are utilized to provide high-efficiency optoelectronic devices that could not be achieved using conventional 3D materials.[76–86] For example, a photoelectrochemical photodetector based on liquid exfoliated lew-layered InSe nanosheets with enhanced stability was presented, taking advantage of the bandgap provided by few 2D-layered materials. The choice of few-layered InSe nanosheets has been determined because of their direct bandgap, excellent transport properties, photoresponse, and simplicity of obtaining (using the liquid-phase exfoliation approach). This photodetector has the advantages of enhanced photocurrent density, responsivity, and cycling stability in KOH solution when subjected to solar irradiation. Moreover, the detection of this photoelectrochemical photodetector can be managed by varying the concentration of KOH and applied potential. Therefore, the physical properties of this device provide a high efficiency of photodetection. Besides, the process of the photodetection, InSe nanosheets can be used in other devices such as dye-sensitized solar cells, water splitting systems, and solar tracking equipments.[87]

Using chemical doping in graphene, it is possible to change the Fermi level, and consequently, the work function. Hence the replacement of metal by graphene in Schottky junction-based solar cells provides enormous advantages and much higher power conversion energy (PCE) regarding metal/silicon interface.

Methodologies for obtaining doped graphene with arsenic and phosphorus have been presented using metal-organic chemical vapor deposition (MOCVD). As a result, it has been found that the value of the phosphor and arsenic doped graphene work function, increased from 4.5 eV (undoped graphene) to 4.7 eV and 4.8 eV, for phosphor and arsenic, respectively.[88]

Other research has shown that the solar cell consisting of graphene/n-silicon Schottky junction, using change in the back contact structure, has a simpler manufacturing process, lower manufacturing cost, and a larger contact area than other graphene/silicon-based solar cells. To increase the PCE value for these solar cells, the poly(methyl methacrylate) (PMMA) residues left in the graphene during the transfer process were removed as much as possible. Due to this cleaning and doping process of graphene, this solar cell presented a PCE value of 14.1%.[89]

It is expected that the size-tunable photon absorption and efficient generation of multiple electron-hole pairs will provide high PCE value for inorganic quantum dot (QD) solar cells (greater than the Shockley–Queisser limit).[90] However, this type of solar cell has poor electron–hole separation and poor transfer of photogenerated electrons to electrodes. The use of graphene as an electron acceptor in this type of solar cell with the multilayered graphene/QD resulted in an incident photon-to-carrier conversion efficiency (IPCE) of around 16% and a photoresponse of 10.8 A/m^2 under 1000 W/m^2 illumination.[91]

Due to the graphene's high transparency, up to four layers of graphene enable the replacement of indium tin oxide (ITO) with graphene, for example, in an organic photovoltaic cell (OPV) as a transparent anode, with comparable performance. Research on organic solar cells has revealed that four graphene layers provided the same sheet resistance (30 Ω per square) of the ITO when they were used as the electrode. Hence, the solar cell using graphene replacing the ITO has presented at least 92% of the efficiency regarding the OPV with an ITO electrode for both normal and angular AM1.5 G illumination.[92]

Perovskite metasurface is a new methodology that can be used to increase the efficiency of photonic devices. Research on photonic interactions involving perovskite layer and an interlayer of photoactive organic material in hybrid perovskites has been carried out in order to enable the obtaining of novel photonic devices, such as, photodetectors, solar cells, light-emitting diodes, nanolasers, displays, waveguides, modulators, and nonlinear optical devices.[93]

10. External voltage applied to graphene sheets

10.1. Back gate voltage

Gate voltage means applying a voltage between an external medium and a single graphene sheet, between two parallel graphene tapes, or between an external medium and one of the parallel sheets, depending on the geometry of the nanophotonic device which is analyzed. Through the gate voltage, it is possible to control the chemical potential of graphene, which can operate in the conduction or valence band, depending on the applied voltage, due to the diffusion of negative

(positive) charges in the graphene plasmonic system (electric field effect).[94]

In Fig. 23, we show an example of a scheme for obtaining a gate voltage between silicon and a graphene sheet. In this case, the graphene sheet has been deposited on the silicon oxide substrate with a well-defined thickness, which is supported by highly doped silicon. As the highly doped silicon functions similarly to a metallic contact, silicon dioxide is an insulator, and graphene is a zero-gap semimetal, an electric field effect occurs, similar to that occurring within a capacitor of flat plates so that it is possible to control the charge density in graphene.

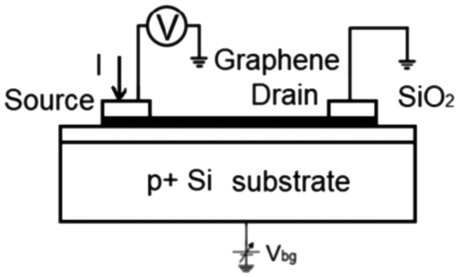

Fig. 23. Back gate voltage between a silicon substrate and a graphene sheet.

This type of gate voltage, called back gate voltage, can be used in graphene-based nanophotonic devices, such as a transistor, whose schematic representation is shown in Fig. 23. As we can see in this figure, from the transistor, it is possible to measure the dependence of conductivity and resistivity of graphene as a function of the voltage between silicon and graphene (in this case, back gate voltage). Note that the electrode located on the left side of Fig. 23 acts as the source, while the other electrode acts as the drain. Then, by applying an alternating current between the source and the drain, and making the measurements of the voltage between the source and drain, for the value of the applied back gate voltage ($V_{\rm bg}$), we obtain the graphs related to the conductivity ($V_{\rm bg}, \sigma$) and resistivity ($V_{\rm bg}, \rho$) of graphene,[95] as shown in Fig. 24.

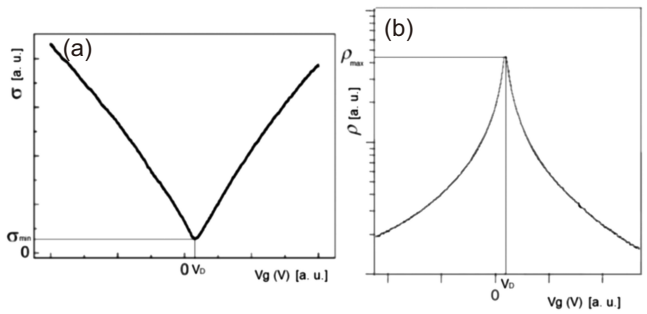

Fig. 24. (a) Example of conductivity versus gate voltage for a graphene channel transistor. (b) Example of resistivity versus gate voltage.

The conductivity of graphene increases (while obviously, the resistivity decreases) as the absolute value of the back gate voltage increases, regardless of whether the voltage applied to the highly doped silicon is positive (and negative in graphene, causing electron transfer to graphene) or negative (and positive in graphene, causing the transfer of holes to graphene).

The position of the Fermi level, whose value is practically the same as the chemical potential of graphene, is controlled in this case by the back gate voltage $V_{\rm bg}$. It is noteworthy that considering graphene as ideal, for $V_{\rm bg} = 0$ eV graphene would have the minimum conductivity ($\sigma_{\rm min}$). However, considering real graphene, the minimum conductivity does not occur under this condition, given the unwanted doping of the graphene from the environment and the device manufacturing process, among other factors.

The Dirac voltage ($V_{\rm D}$), i.e., the gate voltage where the minimum conductivity (or maximum resistivity), for example, in graphene on SiO_2 occurs, has been studied in several experiments, where the influence of the manufacturing and cleaning process of graphene was verified. Additionally, at the interface, there are energy states that behave as charge acceptors or donors. Therefore, there are different values for the graphene Dirac voltage.[96–100] It is noteworthy that the residual charge density in graphene n_0 has typical values between $\sim 5 \times 10^{10}$ cm^{-2} to $\sim 30 \times 10^{10}$ cm^{-2} (p-type doping), for graphene on SiO_2/Si depending on the charge impurity density in SiO_2.[101] So, even without gate voltage, graphene has a residual charge density and for this reason, it is necessary to exclude this charge density from the value of the charge density provided by the gate voltage as shown in Eq. (58).

In the case of back gate voltage, considering graphene and highly doped silicon surface, such as the plates of a flat capacitor and SiO_2 as the dielectric between the plates, the density of graphene charge carriers due to the application of $V_{\rm bg}$ is given by

$$n_{\rm Vbg} = \frac{C_{\rm ox} V_{\rm bg}}{e} - n_0 = \frac{\varepsilon_d \varepsilon_0 V_{\rm bg}}{de} - n_0, \tag{58}$$

where $C_{\rm ox} = \varepsilon_d \varepsilon_0 / d$ is the capacitance per unit area of the graphene/SiO_2/ Si (oxide capacitance) structure, d and $\varepsilon_d = 39$ are the thickness and the dielectric constant of the SiO_2 layer, respectively. It is noteworthy that in Eq. (58) the quantum capacitance of graphene was not taken into account, as will be detailed below, since for dielectric thickness greater than 200 nm, for example, this quantum capacitance can be neglected.[102]

On the other hand, the graphene conductivity can be, theoretically, determined from a semiclassic diffusive transport model according to the following equation:

$$\sigma_{\rm g} = e n_{\rm t} \mu, \tag{59}$$

with $n_{\rm t}$ being the density of graphene charge carriers ($n_{\rm t} = n_0 + n_{\rm Vbg}$) and μ the mobility of these graphene charge carriers.

10.2. Top gate voltage

Considering that practically all potential difference occurs in the dielectric medium, which in a back gate struc-

ture has a large thickness, a large potential difference (ddp) is needed to obtain moderate increments of charge density. However, the application of high values (ddp > 100 V) causes the damage of SiO_2. Therefore, as we have mentioned above, we can state that the back gate voltage process is limited. To overcome this problem, it is necessary to decrease the thickness of the SiO_2 layer, but obtaining thinner layers of this dielectric to support the graphene layer requires more advanced techniques. Another solution is to use a medium with high dielectric constant, such as HfO_2. Thus, the most used solution is the application of a top gate voltage on graphene, so that the dielectric has a small thickness.

One option for improving the top gate voltage efficiency is to replace SiO_2 with h-BN, the thickness of the h-BN layer being thin enough (usually between 10 nm and 20 nm), to increase the efficiency of charge generation in graphene. Figure 25 shows an example scheme for obtaining a top gate voltage between silicon and a graphene sheet.

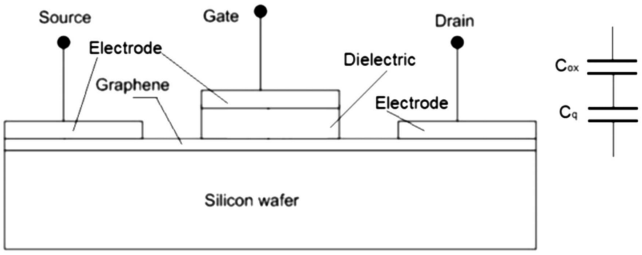

Fig. 25. Schematic representation of a top gate voltage model.

In the top gate voltage structure, a graphene sheet shall be deposited on the silicon, and the insulator shall be deposited above the graphene so that the insulator is in contact with the gate electrode. Since in this case, the dielectric thickness is small (generally 5 nm to 15 nm), the quantum capacitance per unit area cannot be neglected. As the quantum capacitance (C_q) is inherent to the graphene layer, we should consider the total capacitance per unit area of the structure (C_t) shown in Fig. 25 as a series association of C_{ox} and C_q. C_q is given by[103]

$$C_q = \frac{2e^2}{\hbar V_F}\sqrt{\frac{|n_{Vtg}+n_0|}{\pi}}, \tag{60}$$

considering $eV_{ch} \gg K_B T$, where n_{Vtg} is the charge density provided by the top gate voltage. Therefore,[104]

$$C_t = \frac{2C_{ox}e^2|n_{Vtg}+n_0|}{2e^2|n_{Vtg}+n_0| + C_{ox}\hbar V_F\sqrt{\pi}}, \tag{61}$$

with

$$n_{Vbg} = \left(\frac{eV_{ch}}{\hbar V_F\sqrt{\pi}}\right)^2. \tag{62}$$

Here, V_{ch} is the voltage on the channel (over graphene), which depends on the potential difference between the source port and the drain port (V_{ds}), as well as on the potential difference between the gate electrode and the source port (V_{gs}).

10.3. Top gate voltage + back gate voltage

An even more efficient system for applying gate voltage is the simultaneous use of a back gate voltage and a top gate voltage, according to the schematic representation shown in Fig. 26.

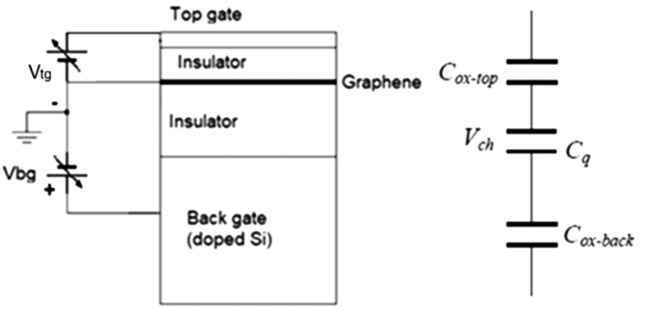

Fig. 26. Schematic representation of the application of a top gate voltage simultaneously with the application of a back gate voltage.

Top gate + back gate experiments were performed using a MOSFET where a graphene film was used as the channel of this transistor (length = 5 μm, width = 1 μm). The graphene film has been grown in metal and transferred to a SiO_2 layer, which was located on a silicon substrate. The dielectric used in the top gate was HfO_2 ($\varepsilon_{dt} = 16$) and in the back gate was SiO_2 ($\varepsilon_{db} = 3.9$).[105]

The charge density on the graphene channel (Q_{sh}) has been determined by the hole and electron density difference, multiplied by the elementary charge value.[106] Hence, the capacitance has been obtained by the Q_{sh} derivative concerning the graphene potential, i.e., $C_q = -dQ_{sh}/dV_{ch}$, where $V_{ch} = E_F/e$.

In these studies, it has been found that the minimum quantum capacity at room temperature had a value $C_{qmin} \approx 0.8\ \mu F\cdot cm^{-2}$, without taking into account the intrinsic charge density of graphene. However, considering, for example, $n_0 = 4\times10^{11}\ cm^{-2}$ and $V_{tg} = 0$ V, it has been obtained that $C_{qmin} = 1732\ \mu F\cdot cm^{-2}$.[105]

Note that the total capacity (C_{t2}) per unit area for the double gate voltage device, shown in Fig. 26, is given by the serial association of capacitance per unit area (quantum, top-gate oxide (C_{ox}-top) and back-gate oxide (C_{ox}-back)), i.e.,

$$\frac{1}{C_{t2}} = \frac{\hbar V_F}{2e^2}\sqrt{\frac{\pi}{n_s}} + \frac{t_g}{\varepsilon_t\varepsilon_0} + \frac{t_b}{\varepsilon_b\varepsilon_0}. \tag{63}$$

Here, t_g, t_b, ε_t, and ε_b represent the top-gate dielectric thickness, back-gate dielectric thickness, top-gate dielectric constant, and back-gate dielectric constant, respectively.

Another research used a transistor operating with top gate and back gate together consisting of graphene over Si/insulator, in which the source and drain electrodes (left part of Fig. 27) were made of a gold film with 50 nm thickness and titanium (thickness 5 nm), which presented ohmic contact with graphene less than few kΩ.[107]

Between these two electrodes, a 30 nm thick aluminum film was inserted, which was directly deposited on the

graphene layer and was used as the top gate electrode. It is noteworthy that the insulation between the aluminum film (top electrode) and the graphene layer was not achieved by the introduction of a conventional insulating film. This isolation was achieved simply after this device remained exposed to the air for a few hours.[108] It was shown that the resistance between the top gate electrode and the source and drain electrodes exceeded 100 MΩ, but the interior of the aluminum electrode remained intact and conductive.

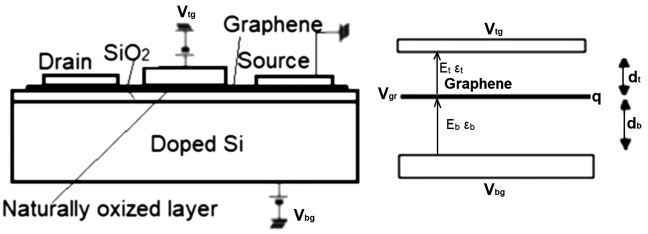

Fig. 27. (a) Schematic representation of a transistor having top gate + back gate. (b) Electric fields and potentials related to the top gate + back gate system of a graphene channel transistor.

The greater possibility of the occurrence of this insulation film (obtained between the aluminum film and the graphene layer) with an estimated thickness between 5 nm and 9 nm is due to the oxygen diffusion present in the atmosphere, and to the very weak physical contact between the aluminum electrode and graphene layer.[109–111]

In Fig. 27(b), we can observe the physical representation regarding the electric fields and potentials through this device. The electric fields and potentials on the graphene channel (V_{gr}) are related as follows: $V_{bg} - V_{gr} = E_b d_b V_{gr} - V_{tg} = E_t d_t$, with V_{bg} and V_{tg} being the applied voltages at the top gate electrode and bottom electrode (highly doped silicon), respectively, E_t and E_b the electric fields between the top electrode and the graphene and between the graphene and the bottom electrode, respectively. By Gaussian law, considering that the graphene layer has charge density q, we can say that $\varepsilon_t d_t - \varepsilon_b d_b = q$, where ε_t is the dielectric constant of the top gate, ε_b is the dielectric constant of the back gate, and d_t and d_b are the dielectric thicknesses for the top and bottom capacitors, respectively. From the above equations, we can arrive at the following equation:[107]

$$\frac{\varepsilon_t}{d_t} V_{tg} + \frac{\varepsilon_b}{d_b} V_{bg} = (1+\alpha)\frac{\varepsilon_t}{d_t} V_{gr} - q, \tag{64}$$

where $\alpha = \frac{\varepsilon_b}{d_b} / \frac{\varepsilon_t}{d_t}$. Note that the value of α corresponds to the value of the ratio between the back gate capacitance and the top gate capacitance per unit area. After some mathematical manipulations, the value of α has been got ($\alpha = 0.013$) by measurements, using the device shownin Fig. 27(a). Hence, taking into account that the SiO_2 dielectric constant is $\varepsilon_b = 3.9$ and the silica layer thickness is $d_b = 300$ nm, the top gate capacitance for this device was estimated to be 8.9×10^{-3} F/m^2. Additionally, assuming that the aluminum oxide dielectric constant has a value between 5 and 9, the top gate dielectric thickness should be between 5 nm and 9 nm. Note that obtaining a dielectric film with this small thickness is very difficult to achieve by using conventional methods.[107]

10.4. Fermi level control via gate voltage

The graphene's Fermi level (approximately the same value as graphene's chemical potential) is related to the voltage applied to graphene (back voltage) according to the following equation:[112]

$$E_F \cong \mu_q = \pm \hbar V_F \sqrt{\frac{\pi \varepsilon_0 \varepsilon_d}{ed} \left| (V_g - V_D) \right|}, \tag{65}$$

where $\varepsilon_0 \varepsilon_d$ is the electrical permittivity of the dielectric and V_D is the Dirac voltage (gate voltage for which the maximum graphene resistivity occurs, or in other words, for which the minimum conductivity of graphene occurs). In Eq. (65), the + sign is used for $V \leq V_D$ and the − sign for $V > V_D$.

Note that for ideal graphene, the gate voltage at which graphene's maximum resistivity occurs is $V_g = V_D = 0$. In an experiment, it was shown that via the dry transfer of graphene films to the standardized substrate (SiO_2/Si), as well as subsequently modified RCA cleaning, devices with low graphene Dirac voltages were obtained, i.e., $V_D < 4.5$ V, with a mean value around 2.5 eV.[113] However, during the investigation of a low flicker frequency in a graphene layer on h-BN/SiO_2/Si as well as on SiO_2/Si, it was found that $V_D \approx 5$ V for graphene on h-BN/SiO_2 /Si and $V_D \approx 25$ V for graphene over SiO_2/Si.[114]

Given the importance of this subject, we will detail the research conducted on gate voltage in a graphene structure over h-BN, which is supported by Cu(111).[115] In this research, the electrostatic doping of graphene, as a function of the applied voltage and the thickness of the h-BN layer, was detailed, using first-principles density-functional theory calculations (DST). It has been observed that even without a gate voltage there is a spontaneous charge transfer between Cu (111) and graphene through h-BN so that graphene maintains intrinsic doping. This charge transfer occurs due to the difference between the work functions of Cu(111) and graphene, but it is strongly altered by displacement of the charges due to the poor chemical interactions at the metal/h-BN interfaces, and h-BN/graphene. However, the application of a variable gate voltage can be used to provide the controlled level of the graphene doping, as it has been shown through other research, where it has been showed that the graphene Fermi level is dependent on the square root of the voltage.[64,116–119]

The structure used in this research has been modeled in a periodic supercell in the normal direction to the plane of the graphene layer (z), with six atomic layers of copper atoms in the surface orientation (111), a thin film with 1 to 6 layers of h-BN, a single graphene layer, and a vacuum region of 15 Å. It has been shown that in this structure (Cu (111)/h-BN/graphene), graphene has intrinsic n-type (electrons) doping. However, the difference between the Fermi level of

this structure and that of the graphene decreases with an increasing number of h-BN layers. This intrinsic doping of graphene originates from the transfer of electrons from copper to graphene via h-BN. The working functions related to copper and graphene, without applying a gate voltage, presented the values $W_M = 5.25$ eV and $W_G = 4.48$ eV, respectively. Therefore, in a structure consisting only of copper and graphene, there is an electron transfer from graphene to copper (average electron energy level in graphene is higher than that in copper), so that in this case, graphene is intrinsically positively doped, i.e., the difference in the graphene Fermi level is positive ($\Delta_{EF} > 0$). However, a great influence of the h-BN layer has been proven, because, in the aforementioned structure, this does not occur. Incidentally, in the Cu(111)/h-BN/graphene structure, the difference between the copper and graphene Fermi levels is $\Delta_{EFCG} = -0.49$ eV (average electron energy level in copper is higher than that in graphene), which means that in this case, in order to achieve equilibrium, it is necessary to transfer electrons from copper to graphene so that graphene receives an intrinsic n-type doping.

The explanation for the above can be seen in Fig. 28. Note that a potential drop occurs at the copper/h-BN interface ($\Delta_{EpMH} = 1.12$ eV), as well as at the h-BN/graphene interface ($\Delta_{EpHG} = 0.14$ eV).

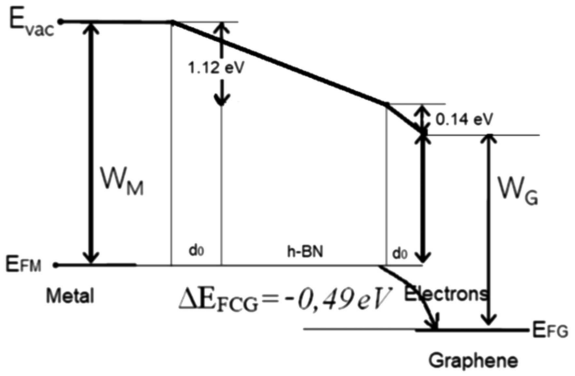

Fig. 28. Schematic representation of the energy levels in the Cu(111)/h-BN/graphene structure.

The energy difference between the two interface media is explained by the formation of dipoles between the two materials (at the interface), which occurs due to the Pauli exchange repulsion principle. In other words, this means that the adsorbed charges on the surface cause repulsions concerning substrate charges so that, in this case, electrons transfer to copper occur.[71,120] It is noteworthy that the intensity of these dipoles does not depend on the number of layers of h-BN, for the number of layers greater than 1.[115] In Fig. 28, d_0 is the average distance between the charges constituting the dipoles.

Note that the difference between copper and graphene Fermi levels is given by $\Delta E_{FMG} = W_M - \Delta E_{pMH} - \Delta E_{pHG} - W_G$. Then, due to charge transfer, a potential difference occurs between copper and graphene so that the h-BN layer is crossed by an electric field, which provides the polarization of the h-BN layer.

On the other hand, by applying a positive gate voltage between copper and graphene, so that an electric field is generated, which opposes the intrinsic electric field mentioned above, it is possible to alter the doping of graphene and consequently its Fermi level. Incidentally, the application of a gate voltage that provides an electric field $E_g = 0,1$ V/Å (contrary to the intrinsic electric field) causes a null electric field in the h-BN layers, so that h-BN behaves as if it were isolated. Obviously, the application of an electric field due to a negative gate voltage causes an increase in the polarization of the h-BN layers. Therefore, the application of gate voltage provides the control of graphene doping, and consequently, its Fermi level.

Through further research, an analytical model has been developed for current tunneling and contact resistivity in a metal/insulating/graphene (MIG) structure using gate voltage, where the metal/graphene (MG) junction can be considered as a particular case of the MIG structure.[121] In this model, a voltage drop has been considered between the insulation edges, i.e., between metal and graphene (ΔV). The reason for this voltage drop across the insulator is the difference between the work functions of graphene (W_g) and metal (W_m), so that a charge transfer between these two materials occurs. Moreover, there is also the influence of chemical interactions between graphene and metal.[122]

The displacement of the graphene Fermi level (E_{Fg}) concerning the energy level at the Dirac point (E_D) as a function of the graphene charge doping is defined as $\Delta E_{Fg} = E_D - E_{Fg}$. In these researches, the relationship between the applied voltage (V) and ΔE_{Fg} is presented as

$$\Delta E_{Fg} = W_m - W_g - e\Delta V - eV. \tag{66}$$

The potential drop at the interface is represented by $\Delta V = \Delta_{tr} + \Delta_{ch}$, where Δ_{tr} is a parameter that determines the influence of charge transfer between metal and graphene, and Δ_{ch} represents the influence of short-range interaction due to the overlap of wave functions in metal and graphene. However, according to Khomyakov's model,[111] the value of Δ_{ch} depends greatly on the separation distance (d) between metal and graphene (insulation thickness), so that it becomes negligible for $d \approx> 4$ nm.

The energy level at the Dirac point ($E_D = eV_D$) can be determined by the following equation:

$$E_D = W_m - W_g - \Delta_{ch} \rightarrow V_D = \frac{W_m - W_g - \Delta_{ch}}{e}. \tag{67}$$

After some mathematical manipulations, the variation regarding the Fermi level due to a gate voltage application is given by[121]

$$E_F = \pm \frac{\sqrt{1 + 2\alpha q|V - V_D|}}{\alpha}, \tag{68}$$

where $\alpha = 2q^2 x/\varepsilon_0 \varepsilon_d \pi \hbar^2 V_F^2$, with $x = d$–d_0 being the effective distance between graphene and semiconductor charges (which form the dipole) and V_F the Fermi velocity. The d_0 represents

the offset of the charges that form the dipole at the interfaces M/I, and G/I (in this case, $d_0 = 0,24$ nm). The $+$ and $-$ values in Eq. (68) have the same meanings given in Eq. (65), i.e., the $+$ sign is used for $V \leq V_D$, and the $-$ sign for $V > V_D$.

Although equation (68) has been determined for temperature $T \to 0$, it can be used at room temperature since the values found are approximately the same. In addition, this equation can also be applied to MG structures, which is considered a particular case of the MIG structure. However, while for MIG structures the value of $\Delta_{ch} = 0$, for MG structures (without the intermediate insulator) the value of Δ_{ch} must be taken into account. Additionally, in the MG structure, the equivalent distance (d_e) between interfaces must replace the d value. We will adopt silver as the metal, just to show the detail of this analytical model we are showing. It is noteworthy that for silver, $W_{ag} = 4,92$ eV and $\Delta_{ch} = 0.88$ eV,[111] so that, in this case, according to Eq. (67), for the MIG structure, $V_D = 0,42$ V, and for the MG structure, $V_D = -0,46$ V. This means that in a MIG structure, graphene has intrinsic p-type doping, but in an MG structure, graphene has n-type doping. In Fig. 29(a), we plot the graphene Fermi level displacement as a function of the gate voltage (-2 V to 2 V) relative to the MG structure.

In Fig. 29(b), the graph referring to the MIG structure is shown, where the adopted insulation thickness was 10 nm and the dielectric constant 3.9. For comparison, this plot was elaborated from Eqs. (65) and (68), and as we can see, the values referring to the graphene Fermi level displacement were almost the same.

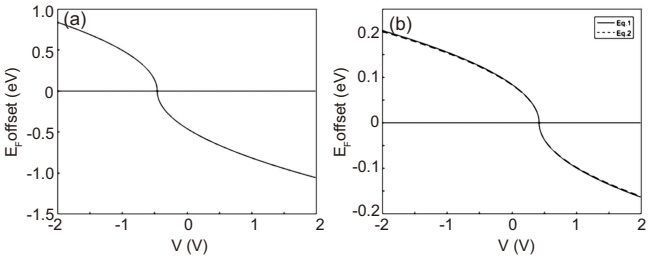

Fig. 29. (a) Fermi level variance as a function of the applied external voltage (-2 V $\leq V \leq 2$ V), referring to the MG structure. (b) That for the MIG structure.

We also plot this same graph for $d = 50$ nm (not shown in Fig. 29) and found that in this case, the Fermi level displacement ranges from approximately -0.08 eV to 0.09 eV. Therefore for this voltage range and insulator thickness greater than 50 nm, we can neglect the displacement of the Fermi level of graphene. However, for higher voltage ranges, this referred Fermi level shift needs to be taken into account.

The possibility of applying a gate voltage to graphene and other 2D materials is perhaps the most important property of these materials. According to we have detailed in this section, it is possible to change the charge density in graphene by a gate voltage, so that a change occurs in its Fermi level[123,124] and consequently in its work function and conductivity. So, managing graphene's work function has many benefits that are not possible to achieve using conventional 3D materials. For example, changing the Fermi level makes it possible to use graphene in increasingly efficient optoelectronic devices such as photodetectors and solar cells. On the other hand, changing the controlled conductivity of the graphene via gate voltage causes the change of its effective dielectric constant so that much more efficient optoelectronic devices, such as waveguides, modulators, and full optical switching cells, among many others, can be obtained. We close this review paper, showing the progress and challenges of tuning concerning the electrical and optical properties of graphene via gate voltage.

For some time now, graphene-based transistors have been researched using back, top, or back and top gate voltage, from low frequencies to infrared.[101,125,126] The gate voltage applied to graphene, operating as the channel in a transistor, changes its Fermi level to the conduction (or valence) band so that its conductivity increases with the addition of electrons (or holes) caused by the application of the gate voltage. Hence, it is possible to control the current flowing between the source and the drain electrodes. It is noteworthy that the gate port, i.e., where we apply the gate voltage, the source and the drain ports are located over graphene.

More recent research has presented a logic inverter based on a transistor consisting of p-doped graphene associated with a transistor made up n-doped graphene. Graphene doping was obtained through lanthanide dopants, and the operation of this device is based on C-H-π interactions between graphene and lanthanide dopants.[127] This research may lead to the development of new technologies based on interactions of graphene and other 2D materials with aggregates of molecules, or ions, (supermolecules) joined by noncovalent interactions.

Advances in technology regarding fully optical networks depend on obtaining optoelectronic devices which can be integrated into photonic integrated circuits (PICs). A graphene-based nanophotonic Mach–Zehnder interferometer (MZI) has been introduced to work as a signal follower, switch, splitter, and as a multiplexer/demultiplexer, with dimensions that allow integration into PICs. This MZI consists of an input coupler, two waveguides in the middle (one waveguide longer than the other, so that the modes propagating within the MZI undergo a relative phase shift), and an output coupler. As in graphene-based nanoribbon waveguides, it is possible to insert 90° bends we can reach the difference between the lengths of the two waveguides by inserting a bend in one of these waveguides. However, as the bend is very small and made up of two bends (to allow the same direction), changes were made in its shape to avoid attenuations in the propagating optical signal. Apart from the difference in waveguide lengths, the operation of this device is based on the application of a gate voltage, in order to shift the conductivity and the effective dielectric constant of graphene so that it enables the operation of this device as any of the options shown above. It is noteworthy that the input and output couplers have lengths of 80 nm, and the distance between the two graphene nanoribbons is 2 nm. The difference

between the lengths of the two arms has values between 3 nm and 6 nm, which are controlled by the number of carbon atoms located in the propagation direction.[128]

References

[1] Zhou Y, Zhang M, Guo Z, Miao L, Han S T, Wang Z, Zhang X, Zhang H and Peng Z 2017 *Mater. Horiz.* **4** 997
[2] Wirth-Lima A J, Silva M G and Sombra A S B 2018 *Chin. Phys. B* **27** 023201
[3] Shi S, Li Z, Sang D K, Xiang Y, Li J, Zhang S and Zhang H 2018 *J. Mater. Chem. C* **6** 1291
[4] Wirth-Lima A J and Sombra A S B 2012 *Journal of Optics* **14** 105402
[5] Jin C, Lin F, Suenaga K and Iijima S 2009 *Phys. Rev. Lett.* **102** 195505
[6] Liu H, Neal A T, Luo Z, Z Xu X and Tománek D Ye P D 2014 *ACS Nano* **8** 4033
[7] Molle A, Goldberger J, Houssa M, Xu Y, Zhang S C and Buckled D 2017 *Nat. Materials* **16** 163
[8] Manzeli S, Ovchinnikov D, Pasquier D, Yazyev O V and Kis A 2017 *Nat. Rev. Mater.* **2** 17033
[9] Phillips c, Gilburd l, Xiaoji G X and Walker G C 2019 *J. Phys. Chem. Lett.* **10** 4851
[10] Melentev G A, Shalygin V A, Vorobjev L E, *et al.* 2016 *J. Appl. Phys.* **119** 093104
[11] Greffet J J, Carminati R, Joulain K, Mulet J P, Mainguy S and Chen Y 2002 *Nature* **416** 61
[12] Širmulis E, Šilėnas A, Požela K, Požela J and Jucienė V 2014 *Appl. Phys. A* **115** 199
[13] Melentev G A, Shalygin V A, Firsov D A, Vinnichenko M Y and Vorobjev L E 2017 *IOP J. Phys.: Conf. Ser.* **917** 062038
[14] Maier S A 2007 *Plasmonics: Fundamentals and Applications* (Berlin: Springer) p. 223
[15] Yu P Y and Cardona M 2010 *Fundamentals of Semiconductors* (Berlin: Springer)
[16] Holm R T, Gibson J W and Palik E D 1977 *J. Appl. Phys.* **48** 212
[17] Chandrasekhar H R and Ramdas A K 1980 *Phys. Rev. B* **21** 1511
[18] Yu E, Melentev G A, Shalygin V A and Suihkonen S 2017 *J. Phys.: Conf. Ser.* **816** 012004
[19] Lagois J and Fischer B 1976 *Phys. Rev. Lett.* **36** 680
[20] Yang F, Sambles J R and Bradberry G W 1990 *Phys. Rev. Lett.* **64** 559
[21] Cramer T Wanner A and Phys P 1997 *Stat Solidi A* **164** R5
[22] Agranovich V, Benisty H and Weisbuch C 1997 *Solid State Commun.* **102** 631
[23] Ha D T, Thuy D T, Hoa T, Van T T T and Viet N A 2017 *J. Phys.: Conf. Ser.* **865** 012007
[24] Kaliteevski M A, Brand S, Abram R A, Kavokin A and Dang L S 2007 *Phys. Rev. B* **75** 1
[25] Lambright S, Butaeva E, Razgoniaeva N, *et al.* 2013 *ACS Nano* **8** 352
[26] Ming T, Chen H, Jiang R, Li Q and Wang J 2012 *J. Phys. Chem. Lett.* **3** 191
[27] Wang H, Liu T, Huang Y, *et al.* 2014 *Sci. Rep.* **4** 7087
[28] Zhang W, Govorov A O and Bryant G W 2006 *Phys. Rev. Lett.* **97** 146804
[29] Boca A, Miller R, Birnbaum K M, Boozer A D, McKeever J and Kimble H J 2004 *Phys. Rev. Lett.* **93** 233603
[30] Antoine-Vincent N, Natali F, Byrne D, *et al.* 2003 *Phys. Rev. B* **68** 153313
[31] Médard F, Zuniga-Perez J, Disseix P, *et al.* 2009 *Phys. Rev. B* **79** 125302
[32] Achermann M 2010 *J. Phys. Chem. Lett.* **1** 2837
[33] Derkachova A, Kolwas K and Demchenko I 2016 *Plasmonics* **11** 941
[34] Johnson P and Christy R 1972 *Phys. Rev. B* **6** 4370
[35] Derkachova A and Kolwas K 2007 *Eur. Phys. J-Spec Top.* **144** 93
[36] Fang Z, Wang Y, Liu Z, Schlather A, Ajayan P M, Koppens F H L, Nordlander P and Halas N J 2012 *ACS Nano* **6** 10222
[37] Yan H, Li X, Chandra B, Tulevski G, Wu Y, Zhu F, Avouris W and Xia P F 2012 *Nat. Nanotechnol.* **7** 330
[38] Nikitin A Y, Guinea F, Garcia-Vidal F J and Martin-Moreno L 2012 *Phys. Rev. B* **85** 081405(R)
[39] Liu J T, Liu N H, Li J, Li X J and Huang J H 2012 *Appl. Phys. Lett.* **101** 052104
[40] Thongrattanasiri S, Koppens F H L and de Abajo J G 2012 *Phys. Rev. Lett.* **108** 047401
[41] Zhang L, Fu X, Lei M, Chen J, Yang J, Peng Z and Tang W 2014 *Chin. Phys. B* **23** 038101
[42] Chen C, Qiao H, Lin S, *et al.* 2015 *Sci. Rep.* **5** 11830
[43] Mak K F, Sfeir M Y, Wu Y C, Lui H, Misewich J A and Heinz T F 2008 *Phys. Rev. Lett.* **101** 196405
[44] Falkovsky L A and Pershogub S S 2007 *Phys. Rev. B* **76** 153410
[45] Luo X, Qiu T, Lu W and Ni Z 2013 *Elsevier - Materials Science and Engineering: R: Reports* **74** 351
[46] Wang B, Zhang X, Yuan X and Teng J 2012 *Appl. Phys. Lett.* **100** 131111
[47] Christensen J, Manjavacas A, Thongrattanasiri S, Koppens F H L and de Abajo F J G 2012 *ACS Nano* **6** 431
[48] Gusynin V P, Sharapov S G and Carbotte J P 2007 *Phys. Rev. B* **75** 165407
[49] Gan C H, Chu H S and Li E P 2012 *Phys. Rev. B* **85** 125431
[50] Zhan T, Shi X, Dai Y, Liu X and Zi J 2013 *J. Phys. Condens. Matter* **10** 215301
[51] Shao Z G, Ye X S, Yang L and Wang C L 2013 *J. Appl. Phys.* **114** 093712
[52] Jablan M, Buljan H and Soljačić M 2009 *Phys. Rev. B* **80** 245435
[53] Cheng Z, Tsang H K, Wang X, Wong C Y, Chen X K, Shi Z and Xu J B arXiv: 1211.5946v1
[54] Vakil A and Engheta N 2011 arXiv:1101.3585v1
[55] Mikhailov S A and Ziegler K 2007 *Phys. Rev. Lett.* **99** 016803
2013
[56] Bludov Y V, Ferreira A, Peres N M R and Vasilevskiy M I 2013 *International Journal of Modern Physics B* **27** 1341001
[57] Dean C R, Young A F, Meric I Lee C Wang L, *et al.* 2010 *Nat. Nanotechnol.* **5** 722
[58] Laturia A, Van de Put M L and Vandenberghe W G 2018 *2D Mater. Appl.* **2** 6
[59] Murray W A and Barnes W L 2007 *Adv. Mater.* **19** 3771
[60] Koppens F H L, Chang D E and García de Abajo F J 2011 *Nano Lett.* **11** 3370
[61] Bao Q Loh K P 2012 *ACS Nano* **6** 3677
[62] Jarillo-Herrero T and Palacios T 2011 *IEEE Electron Device Lett.* **32** 1209
[63] Wang J Ma F and Sun M 2017 *RSC Adv.* **7** 16801
[64] Xue J, Sanchez-Yamagishi J, Bulmash D, *et al.* 2011 *Nat. Mater.* **10** 282
[65] Young A F, Dean C R, Meric I, *et al.* 2012 *Phys. Rev. B* **85** 235458
[66] Watanabe K, Taniguchi T and Kanda H 2004 *Nat. Mater.* **36** 404
[67] Kubota Y, Watanabe K, Tsuda O and Taniguchi T 1913 *Science* **38** 932
[68] Golberg D, Bando Y, Huang Y, Terao T, Mitome M, Tang C and Zhi C 2010 *ACS Nano* **4** 2979
[69] Bolotin K I, Sikes K J, Jiang Z, Klima M, Fudenberg G, Hone J, Kim P and Stormer H L 2008 *Solid State Commun.* **146** 351
[70] Novoselov K S, Geim A K, Morozov S V, Jiang D, Katsnelson M I, Grigorieva I V, Dubonos S V and Firsov A A 2005 *Nature* **438** 197
[71] Cao H, Yu Q, Colby R, Pandey D, Park C S, Lian J, Zemlyanov D, Childres I, Drachev V, Stach E A, Hussain M, Li H, Pei S S and Chen Y P J 2010 *Appl. Phys.* **107** 044310
[72] Cao H, Yu Q, Jauregui L A, Tian J, Wu W, Liu Z, Jalilian R, Benjamin D K, Jiang Z, Bao J, Pei S S and Chen Y P 2010 *Appl. Phys. Lett.* **96** 122106
[73] Murali R, Yang Y, Brenner K, Beck T and Meindl J D 2009 *Appl. Phys. Lett.* **94** 243114
[74] Matthes L, Pulci O and Bechstedt F 2014 *New J. Phys.* **16** 105007
[75] Kresse G and Furthmüller J 1996 *Comput. Mater. Sci.* **6** 15
[76] Liu Y, Shivananju B N, Wang Y, *et al.* 2017 *ACS Appl. Mater. Interfaces* **9** 36137
[77] Yunzheng W, Feng Z, Xian T, *et al.* 2018 *Laser & Photon. Rev.* **12** 1800016
[78] Wang Y, Huang W, Wang C, *et al.* 2019 *Laser & Photon. Rev.* **13** 1800313
[79] Zhang M, Wu Q, Zhang F, Chen L, Jin X, Hu Y, Zheng Z and Zhang H 2019 **7** 1800224
[80] He J, Tao L, Zhang H, Zho B and Li J 2019 *Nanoscale* **11** 2577
[81] Manderson C A, McLiesh H, Curvello R, Tabor R F, Manolios J and Garnier G 2019 *Sci. Rep.* **9** 11221

[82] Tao W, Kong N, Ji X, *et al.* 2019 *Chem. Soc. Rev.* **48** 2891
[83] Kang Y Najmaei S Liu Z, *et al.* 2014 *Adv. Mater.* **26** 6467
[84] Fang Z, Wang Y, Schlather A E, *et al.* 2014 *Nano Lett.* **14** 299
[85] Fang Z, Thongrattanasiri S, Schlather A, *et al.* 2013 *ACS Nano* **7** 2388
[86] Fang Z, Liu Z, Wang Y, Ajayan P M, Nordlander P and Halas N J 2012 *Nano Lett.* **12** 3808
[87] Li Z, Qiao H, Ren X, *et al.* 2018 *Adv. Funct. Mater.* **28** 1705237
[88] Klein C, Cohen-Elias D and Sarusi G 2018 *Heliyon* **4** 12
[89] Suhail A, Pan G, Jenkins D and Islam K 2018 *Carbon* **129** 520
[90] Kamat P V 2008 *J. Phys. Chem. C* **112** 18737
[91] Guo C X, Yang H B, Sheng Z M, Lu Z S, Song Q L and Li C M 2010 *Angew. Chem. Int. Ed.* **49** 3014
[92] Gan C H, Phua W K, Akimov Y A and Bai P 2013 *IEEE Journal of Selected Topics in Quantum Electronics* **20** 1
[93] Zhang Y, Lim C K, Dai Z, Yu G, Haus J W, Zhang H and Prasad P N 2019 *Phys. Rep.* **795** 1
[94] Vasko F T and Zozoulenko I V 2010 *Appl. Phys. Lett.* **97** 092115
[95] Craciun M F, Russo S, Yamamoto M and Tarucha S 2011 *Nano Today* **6** 42
[96] Goniszewski1 S, Adabi M, Shaforost O, Hanham S M, Hao L and Klein N 2016 *Sci. Rep.* **6** 22858
[97] Nistor R A, Kuroda M A, Maarouf A A and Martyna G J 2012 *Phys. Rev. B* **86** 041409
[98] Moser J, Verdaguer A, Jimenez D, Barreiro A and Bachtold A 2008 *Appl. Phys. Lett.* **92** 123507
[99] Lafkioti M, Krauss B, Lohmann T, *et al.* 2010 *Nano Lett.* **10** 1149
[100] Kong J, Franklin N R, Zhou C, *et al.* 2000 *Science* **287** 622
[101] Pince E and Kocabas C 2010 *Appl. Phys. Lett.* **97** 173106
[102] Das Sarma S, Adam S, Hwang E H and Rossi E 2011 *Rev. Mod. Phys.* **83** 407
[103] Xia J, Chen F, Li J and Tao N 2009 *Nat. Nanotechnol.* **4** 505
[104] Arya R K and Bala T S 2016 *ARPN Journal of Engineering and Applied Sciences* **11** 2
[105] Rahman M T, Roy A K, Bhuiyan H M A R, Islam M T and Bhuiyan A G 2014 1*st International Conference on Electrical Information and Communication Technology IEEE*
[106] Thiele S A, Schaefer J A and Schwierz 2010 *J. Appl. Phys.* **107** 094505
[107] Tsukagoshi K, Miyazaki H, Li S L, Kumatani A, Hiura H and Kanda A 2011 *Graphene And Its Fascinating Attributes* (Sigapore: World Scientific Publishing Co. Pte. Ltd)
[108] Miyazaki H, Li S Kanda A and Tsukagoshi K 2010 *Semicond. Sci. Technol.* **25** 034008
[109] Qi Y, Hector L G J Ooi N and Adams J B 2005 *Surf. Sci.* **581** 155
[110] Ziovannetti G, Khomyakov P A, Brocks G, Karpan V M, van den Brink J and Kelly J 2008 *Phys. Rev. Lett.* **101** 026803
[111] Khomyakov P A, Giovannetti G, Rusu P C, Brocks G, Zan den Brink J and Kelly P J 2009 *Phys. Rev. B* **79** 195425
[112] Xu F, Das S, Gong Y, Liu Q, Chien H C, Chiu H Y, Wu J and Hui R 2015 *Appl. Phys. Lett.* **106** 031109
[113] Abhilash T S, De Alba R, Zhelev N, Craigheadb H G and Parpia J M 2015 *Nanoscale* **7** 14109
[114] Kayyalha M and Chen Y P 2015 *Appl. Phys. Lett.* **107** 113101
[115] Bokdam M, Khomyakov P A, Brocks G, Zhong Z and Kelly P J 2011 *Nano Lett.* **11** 4631
[116] Zhang Y B, Brar V W, Wang F, Girit C, Yayon Y, Panlasigui M, Zettl A and Crommie M F 2008 *Nat. Phys.* **4** 627
[117] Zhang Y B, Brar V W, Girit C, Zettl A and Crommie M F 2009 *Nat. Phys.* **5** 722
[118] Kim L E and K S Kim P 2009 *Nano Lett.* **9** 3430
[119] Decker R, Wang Y, Brar V W, Regan W, Tsai H Z, Wu Q, Gannett W, Zett A and Crommie M F 2011 *Nano Lett.* **11** 2291
[120] Bagus P S, Staemmler V and Wöll C 2002 *Phys. Rev. Lett.* **89** 096104
[121] Chaves F A, Jiménez D Cummings A W and Roch S 2014 *J. Appl. Phys.* **115** 164513
[122] Champlain J G 2011 *J. Appl. Phys.* **109** 084515
[123] Kim B K, Jeon E K, Kim J J and Lee J O 2010 *J. Nanomater. Volume* **2010** 575472
[124] Yu Y J, Zhao Y, Ryu S Brus L E, Kim K S and Kim P 2009 *Nano Lett.* **9** 3430
[125] Nanda B S and Puttaswamy P S 2019 *Int. J. Electr. Comput. Eng.* **9** 4826
[126] Wang H Hsu A Kong J Antoniadis D A and Palacios T 2011 *IEEE Transactions on Electron Devices* **58** 1523
[127] Gajarushi A S, Wasim M, Nabi R, Kancharlapalli S, Rao V R, Rajaraman V, Subramaniam C and Shanmugam 2019 *M Mater. Horiz.* **6** 743
[128] A. Wirth Lima Jr. and Sombra A S B 2017 *Opt. Quant. Electron.* **49** 388